buildings

MDPI

Article

Freeze–Thaw Performance and Microstructural Stability of Alkali-Activated Slag Mortars Incorporating Mussel Shell Waste

Merve Şahin Yön

Department of Civil Engineering, Faculty of Engineering, Munzur University, 62000 Tunceli, Türkiye; mervesahinyon@munzur.edu.tr

Abstract

This study investigates the use of mussel shells (MSs), a biogenic by-product of the food industry, as a partial replacement for ground granulated blast furnace slag (GBFS) in alkali-activated mortars. Given their high $CaCO_3$ content, MSs represent a sustainable secondary raw material that reduces both waste disposal burden and reliance on natural resources, while offering a low-carbon alternative to conventional cement-based binders. Alkali-activated mussel shell/slag mortars (AAMSs) were produced with MS replacement ratios of 0%, 5%, 10%, 15%, and 20% by mass of GBFS. Sodium hydroxide (NaOH) and sodium silicate (Na_2SiO_3) were used as alkaline activators. Fresh specimens were cured at 60 °C for 48 h. The experimental program included workability, compressive and flexural strength, water absorption, porosity, density, capillarity, ultrasonic pulse velocity (UPV), and freeze–thaw (F-T) resistance tests. Increasing MS content slightly reduced flowability and mechanical strength, while increasing water absorption, porosity, and capillarity. The M0 series achieved the highest 28-day compressive strength (54.06 MPa), while M15 exhibited the highest flexural strength (5.23 MPa). Following F-T cycling, the 5% and 10% MS series demonstrated the best compressive strength (30 MPa). The 10% MS exhibits a relatively balanced overall performance, providing the best balance between mechanical performance, F-T resistance, and microstructural stability, as confirmed by scanning electron microscopy (SEM)/energy-dispersive X-ray spectroscopy (EDS) analyses showing elevated Ca/Si ratios and the formation of Ca-rich crystalline phases.

Keywords: alkali-activated mussel shell/slag mortar; freeze–thaw test; mechanical properties; mussel shell

Check for updates

Academic Editor: Mauro Mitsuuchi Tashima

Received: 15 May 2026
Revised: 17 June 2026
Accepted: 22 June 2026
Published: 24 June 2026

Copyright: © 2026 by the author. Licensee MDPI, Basel, Switzerland. This article is an open access article distributed under the terms and conditions of the Creative Commons Attribution (CC BY) license.

1. Introduction

The demand for construction materials at a global level- particularly cement has been driven up by population growth, rapid urbanization and ongoing industrialization. OPC is the most available binder in the construction industry, and its mechanical performance is well known. However, its manufacturing process is very energy-intensive and has great environmental impacts. Around 700–1000 kg of CO_2 is released per ton of cement produced in the process of cement production, mainly due to calcination of limestone and combustion of fossil fuels in rotary kilns [1–3]. Hence, the cement industry alone accounts for approximately 7–8% of the global anthropogenic CO_2 emissions [4–6] and this share is anticipated to increase further with increasing construction activities and the expansion of infrastructure globally [7]. Given these environmental issues, the construction industry is being increasingly required to develop sustainable and low-carbon alternatives to traditional cementitious materials. In this respect, alternative binder systems have

received much attention, providing a way to reduce carbon emissions, while maintaining structural performance. Among them, alkali-activated materials and geopolymer binders are promising candidates due to their lower energy requirements and their ability to incorporate industrial by-products and different waste materials [8–14]. These materials provide a sustainable pathway through valorization of waste and simultaneously reducing the dependence on conventional clinker-based cement systems.

Alkali-activated binders are produced through alkali activation of precursor materials that are rich in aluminosilicates with high silica (SiO_2) and alumina (Al_2O_3) contents. In this process strong alkaline activators such as sodium hydroxide, potassium hydroxide and/or sodium silicate are used to initiate the polymerization reaction. The resulting binder matrix usually displays an amorphous or semi-crystalline three-dimensional aluminosilicate network structure. The performance of alkali-activated systems is highly dependent on several factors such as the raw material type, activator concentration, liquid/solid ratio, curing conditions and the presence of additives [15–21]. Alkali-activated systems are more considered as a viable alternative to OPC for several construction applications due to their high mechanical performance and environmental benefits.

Recently, much attention has been paid to the use of seashell-derived fillers in geopolymer systems due to their positive effects on workability, compressive strength, and the reduction of carbon footprints. Such materials improve the microstructural densification and the overall material performance, thus making the alkali-activated materials more suitable for sustainable construction applications [22–24].

The use of waste materials as partial or total substitution for conventional raw materials in the manufacture of geopolymers has greatly enhanced the environmental value of such systems. Positive mechanical and durability performances have been achieved using industrial by-products like granulated blast furnace slag, silica fume, fly ash and metakaolin [25–28]. Similarly, biological waste materials such as mussel and oyster shells [29,30], and agricultural residues such as rice husk, sugarcane bagasse, and olive pits [31,32] have also shown potential as sustainable constituents in geopolymer systems. Recent years have seen an increasing interest in the partial replacement of traditional binders with shell-based waste materials for their environmental and mechanical benefits [33,34]. Furthermore, Leone et al. pointed out the environmental benefits of recycling mussel shells as secondary raw materials in green construction, emphasizing their role in circular economy strategies [35].

GBFS is one of the main materials used in this study and is a major by-product of the iron and steel industry. It is selected as a binder precursor due to its amorphous structure, high calcium content and high reactivity under alkaline activation conditions. The presence of calcium-rich phases in GBFS that can be transformed to C-S-H gel structures, necessary for strength development [36,37], has led to it being widely regarded as a promising alternative to cement. It is a very efficient component of alkali-activated systems owing to its latent hydraulic properties, especially in combination with other reactive or calcium-containing materials.

Another important material utilized in this study is MS waste. MSs are bivalve biomaterials, mainly composed of calcium carbonate ($CaCO_3$), produced in large quantities from both freshwater and marine aquaculture systems. Production is estimated at about 13.6 million tons per year [38], which has posed considerable environmental and management challenges to the aquaculture industry. The treatment and disposal of shell waste can be expensive and may pollute the environment if not carried out properly [39]. MSs can be used effectively as mineral fillers or supplementary materials in binder systems, but this is due to their high $CaCO_3$ content [40–42]. Pre-treatments such as cleaning, grinding and particle size reduction significantly enhance their reactiv-

ity and dispersion in cementitious matrices. They are of fine particulate structure and positively contribute to the microstructural densification and overall performance of mortar systems [43,44].

The positive influence of using mussel shell powder as a partial replacement or filler in cement-based and geopolymer systems on the refinement of pore structure and durability performance has been confirmed by several studies [45–47].

This study investigates the potential use of waste MS powder as a sustainable supplementary precursor in alkali-activated slag-based mortars. While ground GBFS has been widely utilized in alkali-activated systems, the application of biogenic calcium-rich wastes such as mussel shells has been relatively less investigated, particularly concerning their influence on durability performance under aggressive environmental conditions. In this context, alkali-activated mortars with different ratios of MS powder and GBFS were produced and systematically characterized. The mechanical performance was assessed by the flexural and compressive strength tests, and the durability behavior was assessed by the water absorption and freeze–thaw resistance tests. Moreover, the microstructural features and phase distribution in the mortar matrix were studied by SEM equipped with EDS. The study aims to contribute to the development of environmentally friendly building materials through the valorization of marine shell waste and to provide a comprehensive assessment of its role in alkali-activated mortar systems.

2. Experimental Program

This section deals with the qualities of the binder ingredients utilized in the study, as well as the mixing techniques.

2.1. Materials and Mixture Ratios

Raw materials used for AAMS manufacturing included ball mill-ground MSs and GBFS with particle sizes under 75 μm. The MS was washed to remove sand and salt, then crushed and ground for 20 h. MS was supplied from the Istanbul coastline. GBFS was supplied by Erdemir Steel Factory. GBFS is an industrial waste material with sustainable use potential that can be considered equivalent to cement. The rationale for utilizing MS in AAMS synthesis is its notably high CaO content, given its chemical composition. Table 1 gives the precise chemical oxide composition of MS and GBFS. Natural river sand with a particle diameter of 0–4 mm, water absorption rate of 1.91%, and specific gravity of 2.63 g/cm^3 was used as fine aggregate. The granulometry curve of the aggregate is shown in Figure 1. To make the mixes, a modified polycarboxylate-based polymer liquid superplasticizer (SP) was used. It had a specific gravity of 1.1, could freeze at −10 °C without chloride, and met the requirements of TS EN 934-2 [48]. The proportion of sodium silicate (Na_2SiO_3) to sodium hydroxide (NaOH), utilized as the chemical activator, was 3:1. The sodium silicate used has a silica modulus (MS) (%SiO_2/Na_2O) of 3.1. The liquid sodium silicate contains 9.2% Na_2O and 28.9% SiO_2 and 61.9% H_2O. Vitale et al. [49] investigated the feasibility of using mussel shell powder (MSP), a waste material rich in biogenic calcium carbonate, as a precursor for alkali-activated binders. In the study, two different alkali activator systems were used to evaluate the effect of silica presence in the activation medium on the chemical-mineralogical evolution and mechanical performance of the binders: a 12 M NaOH solution and a combined NaOH-Na_2SiO_3 solution. The purity of the pelletized NaOH was greater than 98% and was prepared at 12 M. The precursor dry contents are shown in Figure 2. The flow chart of the experiments performed is given in Figure 3.

Table 1. Chemical analysis results of MS and GBFS.

Component Name	% Component	% Component
	MS	GBFS
CaO	76.87	36.37
SiO_2	2.91	38.84
Al_2O_3	1.48	15.67
Fe_2O_3	0.31	0.91
MgO	0.01	6.28
Na_2O	0.45	0.43
K_2O	0.00	0.56
SO_3	0.37	-
Specific gravity	2.63	2.89

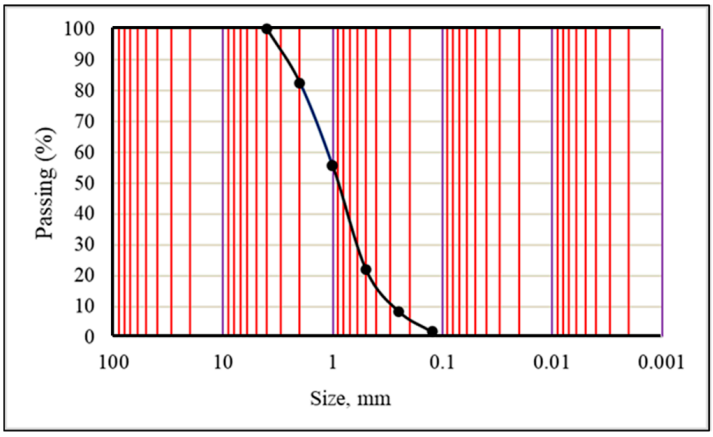


Figure 1. Granulometry curve of sand.



Figure 2. (**a**) MS, (**b**) GBFS, (**c**) Fine sand.

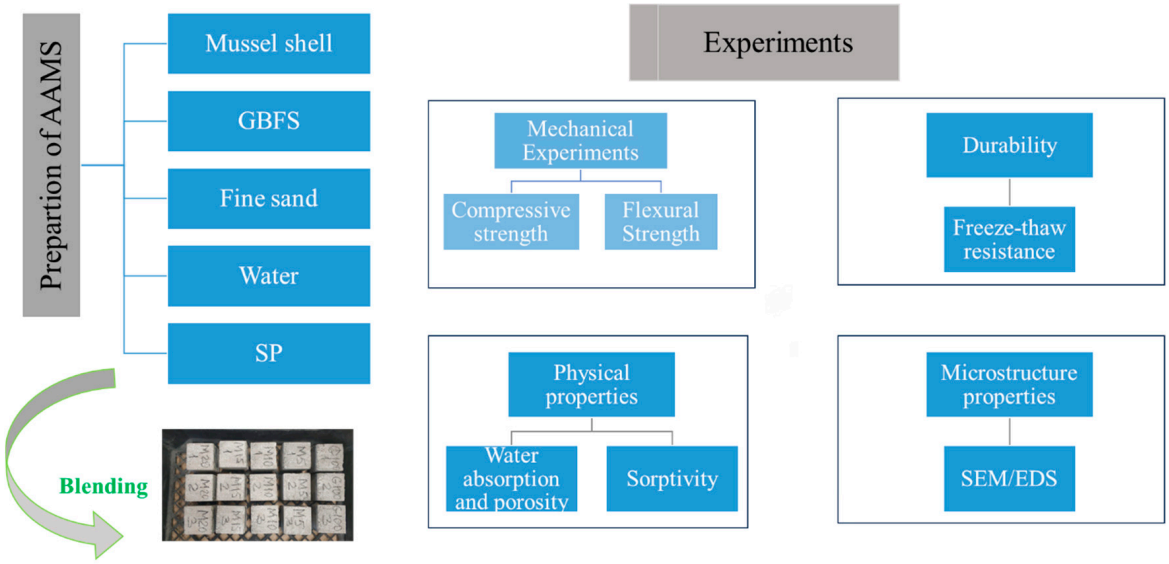


Figure 3. Flowchart summarizing the experimental study.

Characterization of MS and GBFS

X-ray diffraction (XRD) was used to figure out the material properties of MS and GBFS (Figure 4a,b). A Rigaku miniflex600 diffractometer which manufactured by Rigaku Corporation in Akishima, Japan was used to record the XRD patterns of the goods. Cu-K± radiation at 40 kV voltage and 15 mA current was used to hit the samples. The XRD tests were also done at a wavelength of 1.5406 (λ) between 10 and 90°, with a step speed of 0.02° and a scanning speed of 2° per minute. The pink stars are the aragonite phase, and the black dots are the calcite phase in Figure 4a. These are the peaks of the most common calcite phase, which are around 29° to 30° 2θ. The peaks of the aragonite phase are around 26° to 27°, 33°, and 45°. Calcite, which has a very high peak, shows that the mussel shell is made up of a natural mix of calcium carbonate ($CaCO_3$). There are three main types of calcites. Aragonite is one of them. Its peaks are medium in intensity in the picture. Figure 4b depicts the XRD pattern of GBFS, which clearly demonstrates the material's mainly amorphous nature. The pattern's broad, low-density band at 2θ = 25–35° indicates the glass phase-rich structure of GBFS. There are weak peaks on and around the amorphous band that correspond to some low-density but identifiable crystalline phases. These peaks correspond to the phases of Akermanite ($Ca_2MgSi_2O_7$), Gehlenite ($Ca_2Al_2SiO_7$), and Merwinite ($Ca_3MgSi_2O_8$). These phases are silicate and aluminosilicate minerals that are unique to the blast furnace process and match the chemical composition of GBFS.

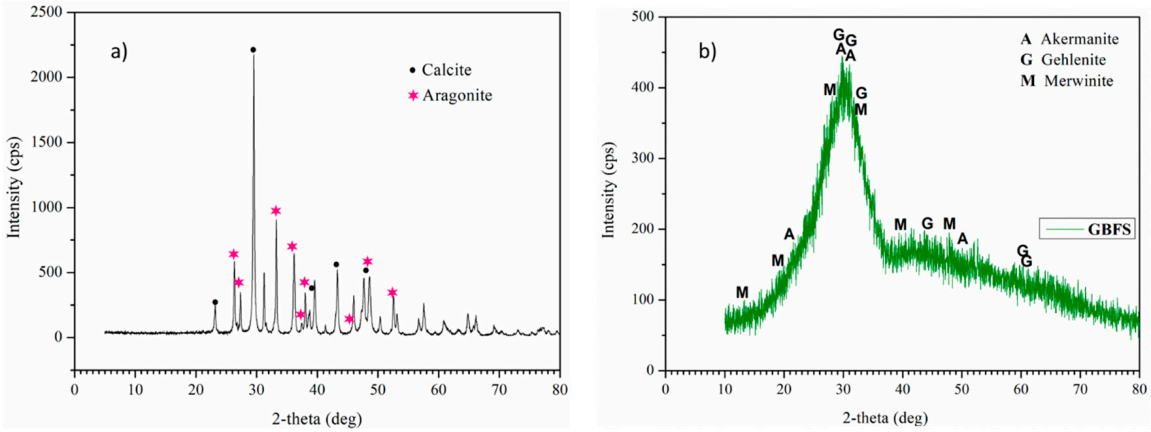


Figure 4. XRD pictures of (**a**) MS and (**b**) GBFS.

The surface morphology was studied using a scanning electron microscope (Hitachi SU3500 which manufactured by Hitachi High-Technologies Corporation in Minato-ku, Japan) and the elemental composition and distribution were characterized by EDS and EDS mapping using an Oxford INCA X-ray spectrometer which manufactured by Oxford-instruments in Oxford, UK. The samples were held in place on a metal holder and wrapped in carbon tapes for SEM/EDS tests. After that, samples were made ready to be measured by covering them with a gold layer. Figure 5a,b shows the SEM images of MS and GBFS at 5000× and 20,000× magnifications. According to Figure 5a particles have a prismatic structure. Figure 5b shows irregular angular particles in the SEM images of GBFS.

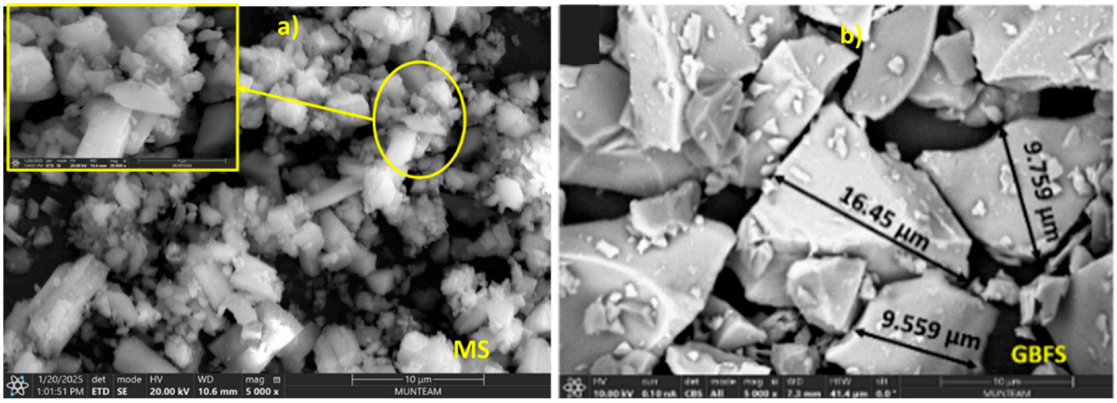


Figure 5. SEM images of (**a**) MS and (**b**) GBFS [50].

Figure 6a shows an overlay map of the elements Ca (red), O (green), and C (blue/turquoise) generated using SEM-EDS elemental mapping images. Calcium, seen in red, is concentrated in the coarse crystalline areas. O, depicted in green, and C, depicted in turquoise, are uniformly scattered across the entire surface. This distribution validates the uniformity of the material's internal structure and the existence of a $CaCO_3$-based framework, as identified by XRD. Figure 6b presents the EDS spectrum of MS powder. The analysis showed that the sample is mainly made of oxygen (O), calcium (Ca) and carbon (C). The EDS results showed that the elemental distribution by weight was 52.1% O, 26.9% Ca, and 20.9% C, respectively. From EDS analysis, these results confirm that the main component of mussel shells is calcium carbonate ($CaCO_3$). The natural shells of mussels are primarily composed of $CaCO_3$ minerals in the form of aragonite or calcite crystals. The absence of an important elemental peak, except for Ca, C and O in the spectrum, indicates that the sample has a calcium carbonate structure with high purity and does not contain significant amounts of foreign elements.

Five distinct mixture designs were created to investigate the impact of MS substitution. The dry materials were measured on a balance with a precision of 0.01 g, subsequently added to the mixing bowl, and manually mixed until homogeneity was attained. Subsequently, SP and water were added to the dry mixture, and NaOH, prepared one day prior to the experiment, was mixed with Na_2SiO_3 and added to the dry mixture. It was mixed first at low speed for 1 min, then at medium speed for 30 s, and finally at high speed for 30 s. In this work, all experimental combinations were generated by triplicate repetitions. MS was replaced with GBFS with a 5% increase in the binder amount by weight from 0 to 20%. The rationale for choosing MS in 5% increments is to assess its impact on the experiments. The AAMS formulation comprised 500 kg/m^3 of binder and a 0.45 alkaline solution/binder (A/B) ratio in all samples. The water/binder (W/B) ratio was kept constant at 0.25 in all mixtures. The amount of water in the alkaline activator solution was not included in the water/binder ratio calculation. Table 2 presents the mixing ratios of the prepared samples.

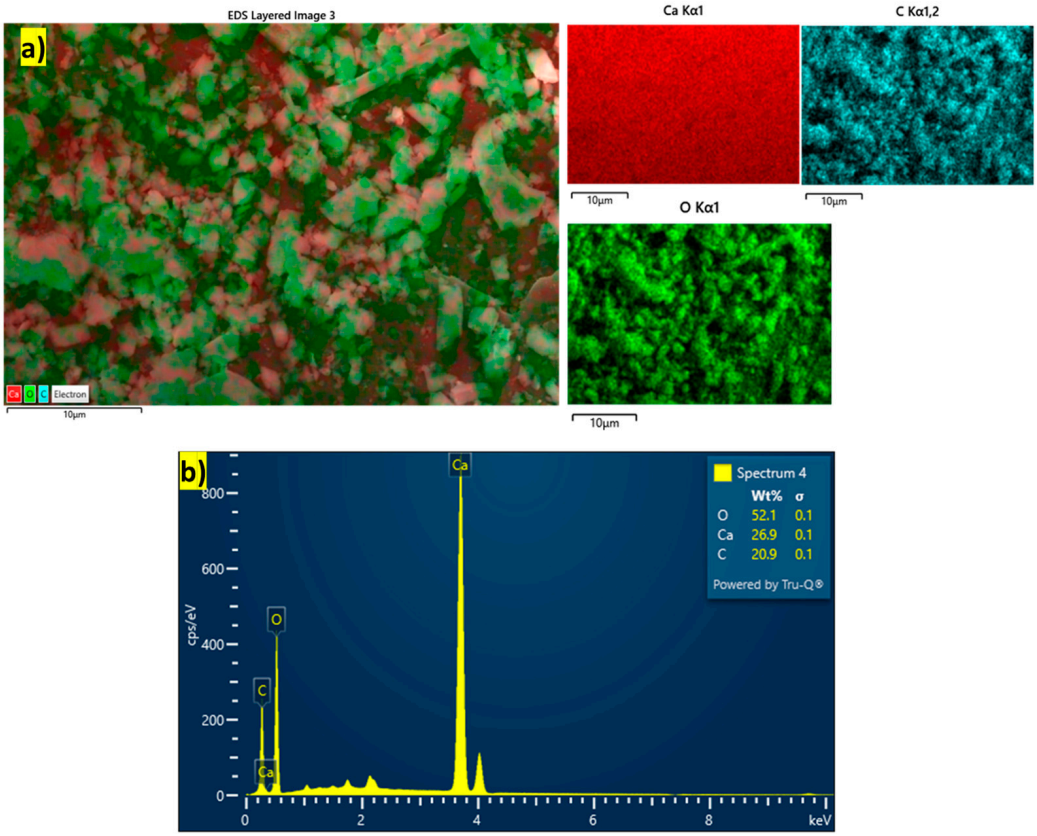


Figure 6. (**a**) EDS mapping and (**b**) EDS results of MS.

Table 2. Mixing ratios of AAMS (kg/m^3).

Codes	Aggregate	MS	GBFS	W/B	NaOH (%)	Na_2SiO_3	SP
M0	1395.65	0	500	0.25	56.25	168.75	8
M5	1398.60	25	475	0.25	56.25	168.75	8
M10	1401.55	50	450	0.25	56.25	168.75	8
M15	1404.49	75	425	0.25	56.25	168.75	8
M20	1407.44	100	400	0.25	56.25	168.75	8

The workability of the AAMS mixtures in the fresh state was evaluated by a flow-cone test performed according to the EFNARC guidelines. The measured spread diameter was in the range of 24 to 26 cm which is sufficient for flowability and consistency for casting and filling of molds without segregation. The values are within the permissible range suggested by EFNARC and confirm that the mixtures have proper fresh-state properties for practical application [51]. The fresh-mixed mortars were cast into molds measuring 40 × 40 × 160 mm for mechanical strength assessment and 50 × 50 × 50 mm to evaluate physical and durability characteristics. The molds were encased in stretch film to inhibit air infiltration, as illustrated in Figure 7. These wrapped samples were immediately exposed to a preheated 60 °C oven cure for 2 days [52]. Subsequent to extraction from the molds, the mortars were maintained at 23 ± 2 °C and 50 ± 5% relative humidity until the experimental day. The mechanical tests were conducted using the Besmak Sematron device which manufactured by Besmak in Ankara, Türkiye at loading rates of 2.4 kN/s for compressive strength and 0.05 kN/s for flexural strength.

This experimental study was conducted in accordance with the standards given in Table 3. In all experiments, 3 samples were taken from the same series and their averages were calculated.

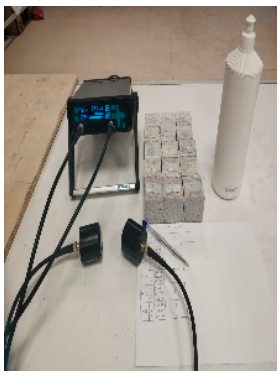


Figure 7. Preserved molds.

Table 3. Attributed standards.

Experiments	Images	Experiments	Images
Compressive Strength [53] Two halves obtained from the flexural test were used to determine compressive strength. All values were obtained as the average of three replicate specimens.		Capillary water absorption [54] Three 50 mm cubic specimens per mix were water-saturated, weighed to 0.01 g precision, and subsequently oven-dried at 105 ± 2 °C to constant mass. The four lateral faces were sealed with waperproof tape to ensure unidirectional water uptake, and capillary absorption was recorded at 5, 10, 20, 30, 60, 180, 360, and 1440 min.	
Flexural Strength [55] Flexural strength was tested on 40 × 40 × 160 mm prismatic specimens aged 3 and 28 days.		Freeze–thaw test [56] F-T cycles were conducted by submerging the samples in water for 2 h during the thawing phase, while the temperature was reduced from +20 to −20 °C over a duration of 6 h for 33 and 100 cycles, respectively.	

Table 3. *Cont.*

Experiments	Images	Experiments	Images
Water absorption, porosity and density [54] Water absorption, porosity, and density were determined using the Archimedes balance, based on the average of three cubic samples over 28 days. Specimen weights were recorded in water, in saturated surface-dry condition, and after oven drying to constant mass.		Ultrasonic Pulse Velocity [57] The UPV test is a non-destructive method that evaluates a material's internal structure and integrity by measuring the propagation speed of ultrasonic pulses through a sample. Transit time (t) between transmitter and receiver probes is recorded, and pulse velocity is calculated as V = L/t, where L is the distance between probes.	

3. Results and Discussion

3.1. Mini-Slump Results

Figure 8 shows the spreading diameters of all AAMSs determined with a constant W/B ratio. At a fixed W/B and SP ratio, the substitution of MS with GBFS from 0 to 20% provided the limit values specified by EFNARC (240–260 mm). The illustration indicates that the substitution rate of MSs in AAMSs has a notable although constrained impact on processability. Sample M0, the reference mixture, demonstrated optimal fluidity, achieving the maximum mini-slump diameter of 254 mm. With an increase in MS ratio to 5%, the mini-slump diameter diminished to 247 mm; at substitution rates of 10% and higher, the measurements stabilized around 244 mm. The glass-phase-rich structure of GBFS dissolves in an alkaline environment, enhancing fluidity, while the inert nature of MSs physically retains some free water, restricting the spreadability of the fresh mixture. Hasnaoui et al. produced three mortars with seashell waste/activator ratios of 2.5, 3, and 3.5 using alkali-activated seashell waste (AASW). Researchers found that increasing this ratio decreased the flow rate [58]. In another study by Wu et al., a decrease in workability and slump values was observed as the seashell powder content increased [59].

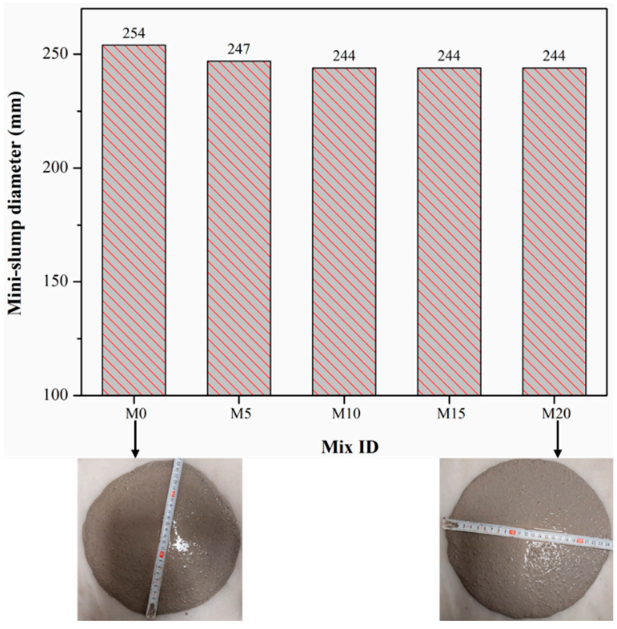


Figure 8. Mini-slump diameter values.

3.2. Flexural and Compressive Strength Results

Figure 9a,b illustrates the flexural and compressive strength values of AAMSs at 3 and 28 days.

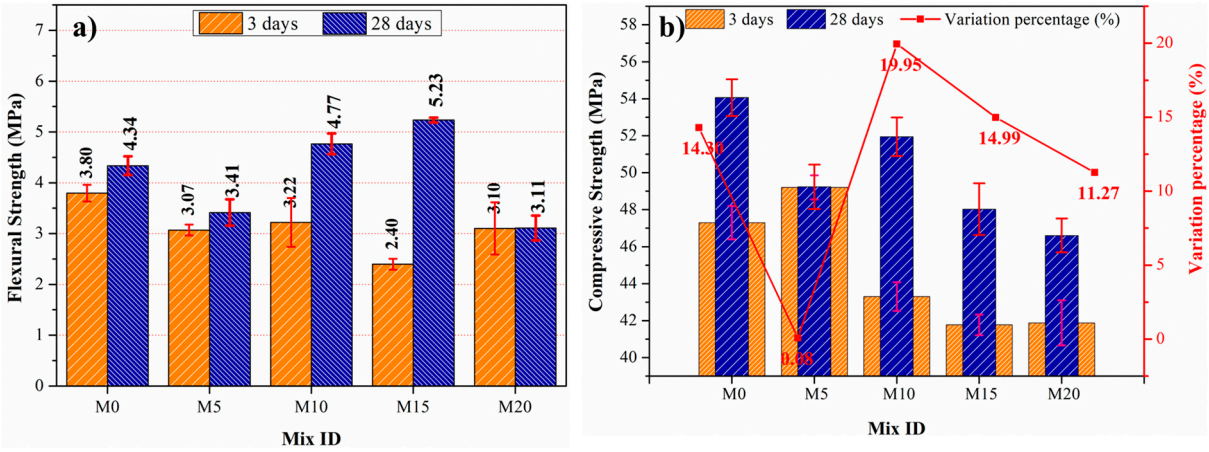


Figure 9. (**a**) Flexural strength and (**b**) compressive strength.

As shown in Figure 9a, the 3-day flexural strengths of the mixtures belonging to the M0, M5, M10, M15, and M20 series were obtained as 3.80, 3.07, 3.22, 2.40, and 3.10 MPa, respectively. However, the 28-day flexural strengths for the M0, M5, M10, M15 and M20 series were measured as 4.34, 3.41, 4.77, 5.23 and 3.11 MPa, respectively. The most significant strength enhancements were observed in the M10 and M15 series. The increases are 48.2% for the M10 series and 117.9% for the M15 series, respectively. It has been determined that there is very little change in the M5 and M20 series. The reduction in flexural strength as the MS content reaches 5% can be attributed to its inferior reactivity relative to GBFS, hence constraining the continuity of the binder matrix during the initial phase. Nonetheless, augmentations in flexural strength through the elevation of the MS ratio to 10% and 15% indicate that mechanical performance can be enhanced. Flexural strength is related to the hydration and bonding of the mortar. This binding is attributed to the reactivity and oxide composition of the material used [60]. The increases in flexural strength observed at 10% and 15% MS replacement ratios can be attributed to several interrelated mechanisms. The high $CaCO_3$ content of mussel shells promotes the formation of additional C-S-H and C-A-S-H gel phases within the alkali-activated matrix, enhancing interfacial bonding between the binder paste and aggregate particles and thereby improving resistance to tensile bending stresses [61]. The irregular surface morphology of MS particles further contributes to mechanical interlocking with the geopolymer matrix, facilitating crack bridging and energy absorption under flexural loading [62]. However, beyond 15% replacement, the excess $CaCO_3$ dilutes the reactive slag content and disrupts the continuity of the geopolymer network, which accounts for the decline in flexural strength observed at the 20% replacement level.

As seen in Figure 9b, the early-age compressive strength of all series exceeds 40 MPa. This demonstrates the successful performance of the GBFS replacement of MS in compressive strength. The 28-day compressive strength of all series exceeds 45 MPa. In comparison to the 3-day compressive strength, the 28-day compressive strength exhibited increases of around 14%, 20%, 15%, and 20% for M0, M10, M15, and M20, respectively; whereas the M5 series showed no variation. AAMS with 0% MS, attained a compressive strength of roughly 47 MPa after 3 days, which rose to 54 MPa after 28 days. The compressive strength of mixes with 20% MS was around 42 MPa at 3 days, increasing to 46.6 MPa at 28 days. The compressive strength exhibited a declining trend as the percentage of MS increased from 0% to 20% in conjunction with GBFS. The reductions in 28-day compressive strength

corresponding to percentage variations in MS from 5% to 20% were 8.9%, 3.9%, 11.15%, and 13.80%, respectively. Based on these results, the optimal percentage change in MS is established at 10%, yielding a compressive strength of roughly 52 MPa.

The reduction in compressive strength at higher levels of MS replacement is in line with earlier studies on $CaCO_3$-rich materials in alkali-activated systems [63,64]. Such behavior can be explained by the dilution of the reactive binder phase and the increase in the specific surface area that may damage the interfacial transition zones in the matrix. The addition of MS resulted in a slight decrease in the compressive strength, but all the mixtures showed acceptable workability and achieved satisfactory strength levels with a significant increase in the use of waste-derived materials.

Also, limestone powder (LP), another additive rich in $CaCO_3$, has shown similar results in alkali-activated systems. It was previously proved that the increase in LP content over 15–20% led to the decrease in strength development due to the lower amount of hydration products formed in the alkali-activated matrix. A similar trend was also observed in the present study, with the maximum strength loss in the mixtures with 15–20% MS. This means that if too much of the $CaCO_3$-rich materials are incorporated, the formation of strength-contributing reaction products may be reduced [65]. On the other hand, studies on alkali-activated materials containing steel slag have reported an increase in compressive strength due to the formation of additional calcium silicate hydrate (C-S-H) gels with better binding properties [66]. The strength development achieved in the present study is in agreement with these findings and indicates that the mechanical performance of the mixtures is strongly influenced by the type and quantity of reaction products formed during the alkali-activation process.

3.3. Water Absorption, Porosity and Density Results

Figure 10 shows the apparent porosity and water absorption data at different MS ratios. The sample M0 exhibited the lowest porosity and water absorption. Sample M15 had the greatest porosity and water absorption. In general, increasing the MS ratio up to 15% increased porosity and water absorption. The augmentation in apparent porosity values relative to M0 is 5.44%, 2.51%, 10.40%, and 7.11% for M5, M10, M15, and M20 samples, respectively, whilst the increase in water absorption capacity is 6.92, 3.07, 12.44, and 9.08, respectively. As can be understood from these numerical data, the 15% MS ratio caused the highest porosity and the highest water-absorbing structure in the sample. As the ratio of MS rises, the quantity of gel produced diminishes, signifying an increase in open and interconnected capillary spaces.

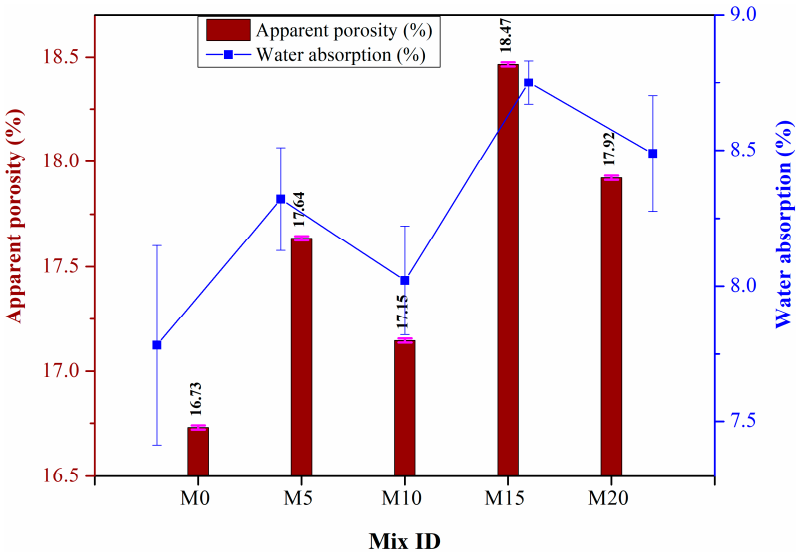


Figure 10. Apparent porosity and water absorption values of the samples.

Figure 11 indicates that the apparent density values for all AAMS range from 2.57 to 2.59 g/cm^3. The M5 and M20 series have the lowest apparent density values, while the M15 series has the highest value. The MS substitution was found to have no substantial impact on apparent density. The saturated surface dry density values range from 2.29 to 2.32 g/cm^3, as illustrated in the picture. The maximum value is 2.32 at M0, while the minimum is 2.29 at M15 and M20. The reduced saturated dry surface densities in M15 and M20 samples suggest greater porosity, as evidenced by their porosity values. And the standard deviations for mixtures M5, M10, M15, and M20 are 0.

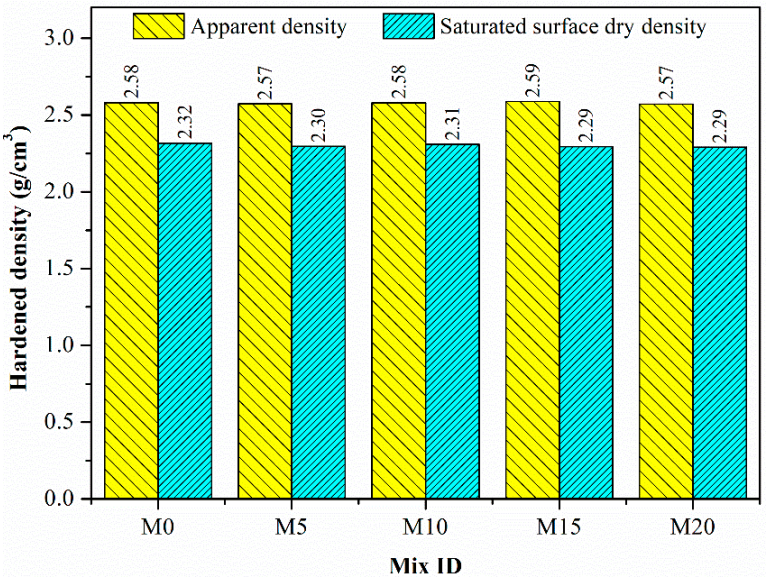


Figure 11. Hardened density of all AAMSs.

3.4. Capillary Water Absorption Results

It has been reported that increases in porosity and capillary absorption in alkali-activated systems containing various waste additives are closely related to variations in strength and durability performance [67].

In this study, the effect of additive materials on capillary water absorption is shown in Figure 12. The capillary water absorption coefficient for the reference mixture (M0) was 4.38×10^{-3} cm/s$^{0.5}$. The addition of MS had no significant effect on the capillary water absorption behavior of the alkali-activated mortar mixtures, as all the capillary water absorption values were in a narrow range from 4.33×10^{-3} cm/s$^{0.5}$ to 4.84×10^{-3} cm/s$^{0.5}$. The capillary water absorption increased slightly with the addition of 5% MS to 4.53×10^{-3} cm/s$^{0.5}$, which is an increase of around 3.4% compared to the reference mixture. However, the lowest capillary water absorption coefficient (4.33×10^{-3} cm/s$^{0.5}$) was obtained for the M10 mixture, which was slightly lower than the control mixture. The filler effect of the fine-dispersed MS particles caused a denser matrix by filling the microvoids in the alkali-activate network. Further increase in MS content caused small increases in capillary water absorption coefficient. The results obtained for M15 and M20 were 4.75×10^{-3} cm/s$^{0.5}$ and 4.84×10^{-3} cm/s$^{0.5}$, respectively, which are increases by about 8.4% and 10.5% with respect to M0. These increases reflected a gradual improvement in capillary water transport but, overall, the variation between mixtures was relatively small. Hence, the addition of MS did not significantly influence the water absorption properties of the alkali-activated matrix in the studied replacement range.

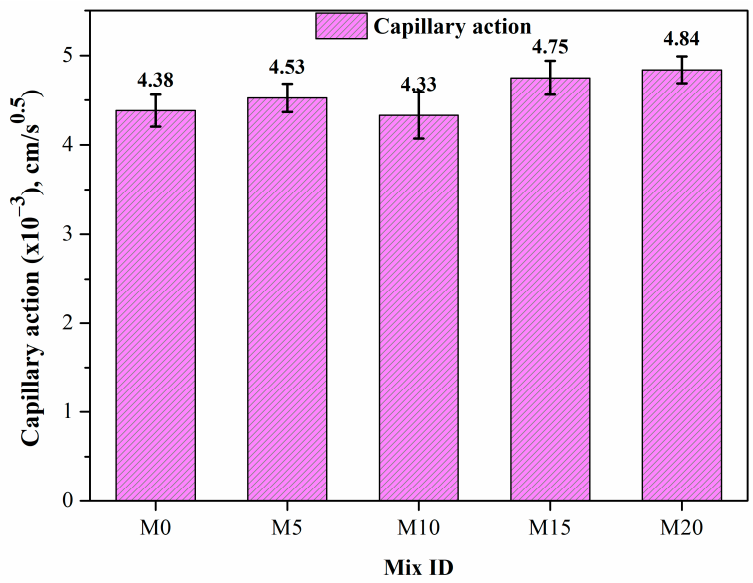


Figure 12. Capillary water absorption coefficient for all AAMSs.

The capillary water absorption behavior is strongly related to the continuity of pores and the development of reaction products within alkali-activated systems. The formation of C-(A)-S-H type gels in the slag-based alkali-activated matrix helps in pore refinement and constrains the water transport. The present results indicate that low and moderate MS replacement levels do not significantly affect gel formation or matrix densification. Also, the standard deviations are small and indicate a good repeatability of the measurements and confirm the reliability of the observed trends.

In summary, the results suggest that the addition of MS up to 20% does not significantly influence the performance of capillary water absorption. Among all the mixtures, M10 exhibited the most favorable capillary absorption behavior and M20 had the maximum capillary absorption coefficient.

3.5. Freeze–Thaw Results

3.5.1. Weight Loss

The average mass changes in all AAMS series after 0, 33 and 100 F-T cycles are presented in Figure 13. The weight losses were relatively limited for all the mixtures, with losses below 2.5% even at 100 cycles of F-T exposure. The weight losses measured after 100 F-T cycles were about 1.90%, 1.50%, 1.70%, 2.43% and 2.46% for M0, M5, M10, M15 and M20 series respectively. The least weight loss was recorded in M5 which shows limited addition of mussel shell powder has positive effect on F-T resistance. This behavior can be attributed to the filling effect of finely ground MS particles, which may partially improve the pore structure. Similar findings were observed by Wu et al., who reported an increase in F-T resistance at low levels of mussel shell powder substitution due to microstructural densification [59]. Further increase in the MS content above 15% resulted in a gradual increase in mass loss, in accordance with the previously observed increases in porosity and capillary water absorption. Severe F-T damage in alkali-activated cementitious materials only occurs when changes in pore structure are accompanied by gel loss and degradation. Higher open porosity allows higher water absorption, which expands during freezing and generates internal hydraulic pressure, leading to microcracking and gradual weight loss. Although the mass losses recorded in all series are relatively small, the much larger reductions in compressive strength, especially in the reference mixture M0, suggest that internal gel degradation and microcrack development may occur without significant surface scaling. This behavior is typical for alkali-activated systems based on

slag where F-T damage mainly reduces the integrity of the C-(A)-S-H gel matrix and does not necessarily appear as an extensive loss of external material [37]. The M10 mixture demonstrated balanced behavior, exhibiting limited mass loss while maintaining relatively good mechanical performance after F-T exposure. SEM/EDS observations confirmed that Ca-rich crystalline phases formed in the presence of MS can help maintain gel continuity and limit crack propagation during F-T cycles. This microstructural stability contributes to the improved durability performance observed at moderate levels of MS substitution [29].

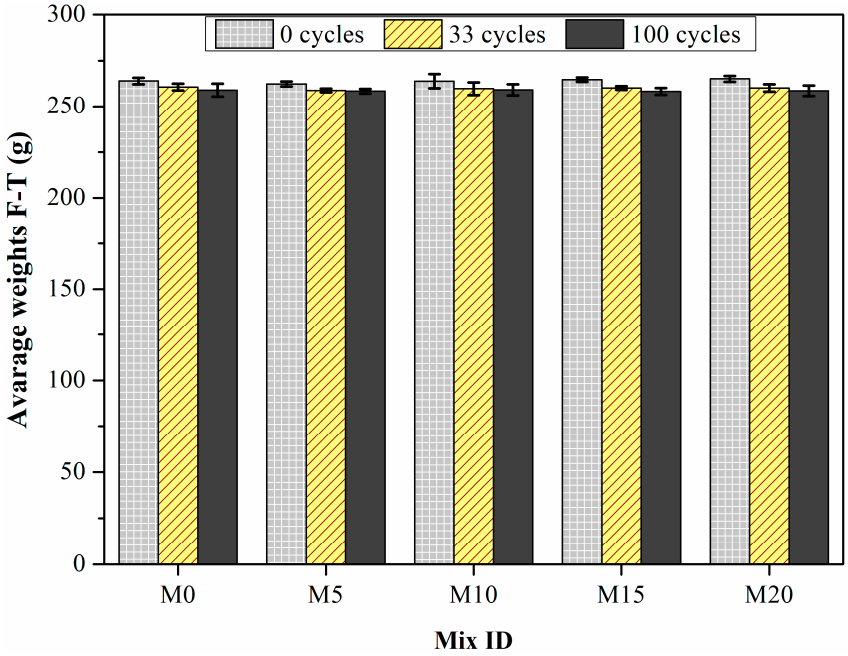


Figure 13. Average weights in AAMSs of F-T cycles.

3.5.2. Ultrasonic Pulse Velocity

Figure 14 shows the UPV measurements of all AAMS before and after 33 and 100 F-T exposures. During the progression of F-T cycle, a decline in UPV values of AAMS was noted. The measured UPV readings for samples M0, M5, M10, M15 and M20 after 100 F-T exposure were 717, 1502, 1206, 1270 and 1014 m/s, respectively. These decreases are 6.59%, 5.87%, 5.15%, 1.63%, 9.44% for M0, M5, M10, M15 and M20, respectively, after 33 cycles, and 64.30%, 21.76%, 37.30%, 29.53%, 45.41% after 100 cycles, respectively. It has been observed that the largest percentage changes occur after 100 cycles. The most significant decline noted in the M0 reference sample after 100 cycles suggests that the gel structure has substantially deteriorated under F-T conditions, resulting in an increase in internal void bonding. Previous research has shown that F-T cycles, pore structure in alkali-activated systems, and slight gel degradation are not sufficient to cause damage [68]. Sample M5 had superior performance, with a 22% reduction in weight loss. The diminished MS ratio produced a filling effect, resulting in a decrease in cavity diameter [69]. The 37% drop noted in M10 aligns with the UPV findings, as will be elucidated in the microstructure evaluation, wherein gel integrity is preserved by calcium-rich needle-like crystals. It should be noted that M20, with its high MS ratio, exhibited a 45% decrease but still performed better than the reference sample. Moreover, the elevated open capillary spaces, indicative of enhanced porosity and sorption, led to increased water expansion upon freezing, hence leading in a reduction in UPV [70].

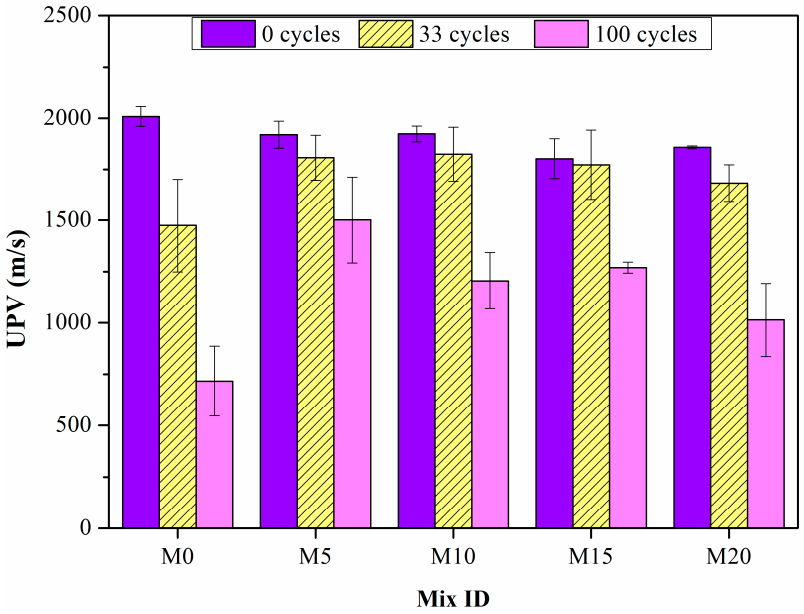


Figure 14. UPV results of all AAMSs.

3.5.3. Compressive Strength After Freeze–Thaw Exposure

Figure 15 presents the compressive strength of all AAMS series before and after 100 F-T cycles and the corresponding percentage changes. Despite the fact that all mixtures experienced a decrease in compressive strength after F-T cycles, the rate of decrease was significantly affected by the MS substitution rate, indicating the interaction of pore structure, gel composition and microstructural stability during the cyclic process. The reference M0 series showed the largest loss of strength, which decreased from about 54 MPa to 20.63 MPa after 100 F-T cycles, a loss of 61.84%. This deterioration indicated that the pure GBFS-based matrix, although it has high initial strength, has a more brittle gel structure with limited resistance to the repeated expansion stresses caused by F-T cycling, as further confirmed by the SEM observations in Section 3.6. Among all the series, the M5 series exhibited the best F-T resistance with compressive strength of approximately 30.38 MPa with a reduction of 38.3%. The improved performance is attributed to the microstructural densification induced by the small amount of MS addition, in which the fine MS particles fill the voids between the particles, refine the pore structure and reduce the amount of freezable water in the matrix. It was demonstrated that alkali-activated slag systems with secondary supplementary materials form a cross-linked gel structure, which leads to a reduction in bound water content and pore water absorption, and thus to a lower susceptibility F-T damage [71]. The M10 series exhibited a strength reduction of 41.45% with a strength of approximately 30.41 MPa, whereas the M15 series showed a reduction of 43.06% and attained a strength of around 27.35 MPa. These reductions were higher than those of M5 but strengths of both series were still significantly higher than that of M0 confirming the beneficial effect of moderate MS incorporation. The M10 series, which has a similar strength to M5, is particularly interesting. The formation of Ca-rich crystalline phases was confirmed by SEM/EDS analysis, which maintained the continuity of the gel and suppressed the propagation of cracks during cycling. Among the series containing MS, the M20 series lost the maximum strength (46.03%) and had a strength of 25.15 MPa which agreed with its higher porosity and capillary water absorption. Higher porosity in alkali-activated slag systems accelerates the formation of F-T damage due to the repeated ice crystallization pressure within the capillary pore network. This circumstance aligns with the observation that the elevated MS ratio, along with heightened porosity and water absorption, as well as an increased capillary water absorption coefficient, has led to augmented microcrack

formation due to water expansion during freezing [72]. Nevertheless, the strength of M20 still substantially exceeded that of M0, suggesting that even at the highest MS replacement level, the calcium-rich secondary phases present in the matrix may provide a degree of microstructural protection against F-T degradation.

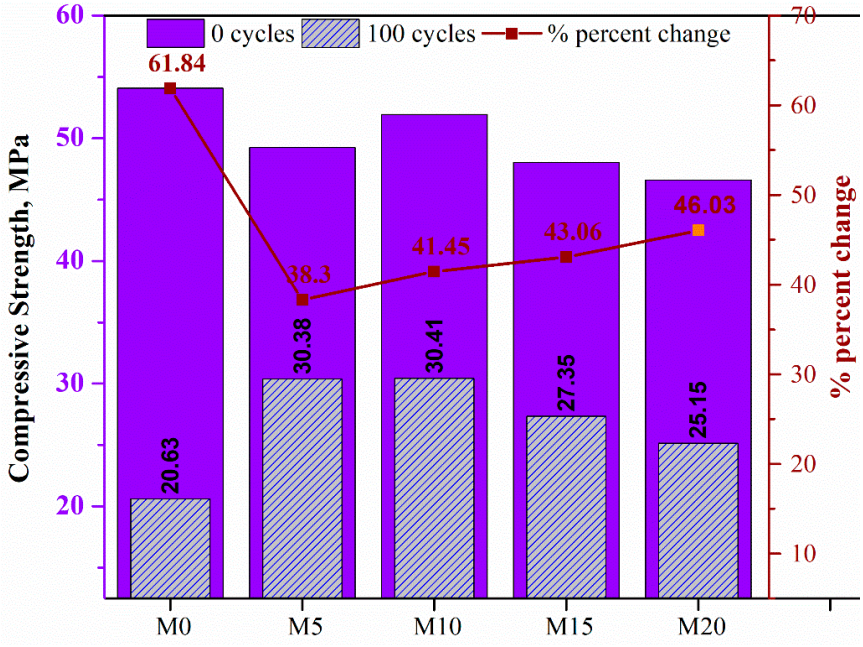


Figure 15. Compressive strengths of AAMS before and after F-T cycles and percent change.

Overall, the optimum replacement ratios of MS were in the range of 5–10% to achieve a balance between mechanical performance and F-T durability.

3.6. Morphological and Elemental Characterization

The effect of incorporation of MS on the microstructural evolution of alkali-activated slag mortars was investigated using SEM/EDS analyses of the control mixture (M0) and the mixture with 10% of (M10) before and after F-T exposure. The SEM micrographs and elemental mapping results of the control mixture (M0), which is composed of GBFS only as the precursor material, are shown in Figure 16a,b. The microstructure is characterized by the presence of a dense and continuous gel-matrix that can be attributed to the formation of calcium–aluminosilicate–hydrate [C-(A)-S-H] gels generated during alkali activation of slag. The presence of Fe and Mg-rich phases dispersed in the matrix is consistent with previous studies on alkali-activated slag systems and suggests the incorporation of these elements into secondary hydration products. These phases contribute to the refinement of the pore structure and improve the chemical stability of the matrix under alkaline conditions. The literature indicates the presence of these zones in alkaline active slag-based systems [73,74]. The persistence of the Ca-Si-Al primary binder gel phase correlates with mechanical performance, while Mg-Al serves as secondary phases that enhance stability in alkaline conditions.

The elemental mapping results in Figure 17 reveal a homogeneous distribution of Ca, Si and Al in the matrix. The uniform distribution results in the formation of a well-connected C-(A)-S-H gel network which is the main contributor to the strength development in alkali-activated slag systems. In contrast, Mg and Fe are found to be localized, indicating their incorporation into secondary reaction products rather than the primary binding phase. Moreover, no significant Na-rich deposits were observed, indicating effective consumption of the alkaline activator in the geopolymerization reaction and, thus, lower probability

of efflorescence-induced degradation. Figure 18 illustrates the principal constituents of the microstructure in sample M0, together with their respective weight percentages as ascertained using EDS spectrum analysis: O (46.4%), Ca (16.9%), C (7.4%), Si (15.7%), Al (5.2%), Na (3.4%), Fe (1.1%), and Mg (2.8%). Prominent high-intensity peaks corresponding to the C-S-H phase are detected in the spectrum for the elements O, Ca, Si, and Al, signifying that calcium, silicate, and hydrate-based reaction products predominate in the mortar composition. The predominant weight percentages of oxygen and calcium suggest that the oxide/silicate gel structures of the binder phases, along with the calcium-rich composition of GBFS, significantly contribute to the alkali activation process. The presence of Ca alongside Si and Al quantitatively verifies the existence of the C-(A)-S-H gel phase. This outcome aligns with the persistent gel matrix identified in SEM and EDS mapping tests.

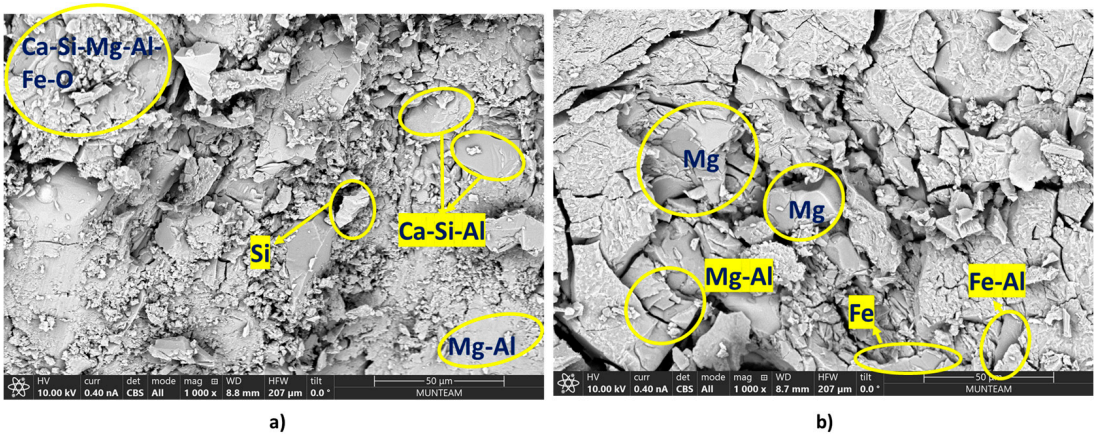


Figure 16. (**a**) SEM image and (**b**) EDS mapping results of M0 specimen (0% MS) cured for 28 days before F-T exposure.

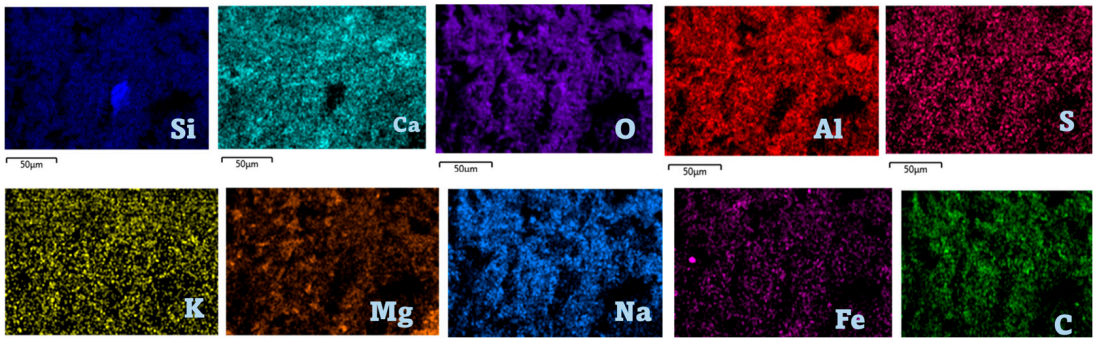


Figure 17. Elemental distribution of M0 mixture cured for 28 days before F-T exposure.

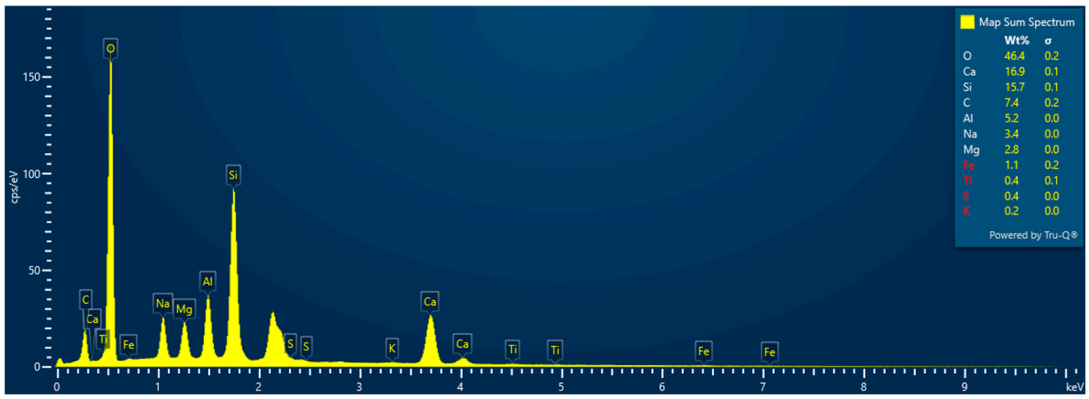


Figure 18. EDS spectrum analysis of M0 sample cured for 28 days before F-T exposure.

SEM images show a dense and interconnected gel structure. This is consistent with the results of the mechanical performance presented in previous sections. The formation of a continuous C-(A)-S-H network helps to improve the matrix integrity, reduce the pore connectivity. Thus, SEM/EDS results not only illustrate the occurrence of alkali activation reactions but also clarify the strength retention.

Figure 19a,b shows the SEM image of AAMS mixture with 10% (M10) and the EDS elemental mapping results. The SEM micrograph shows that the matrix is quite dense and compact, suggesting that the addition of 10% MS did not significantly affect the integrity of the alkali-activated binder system. EDS mapping confirmed the uniform distribution of Ca, Si, Al and O throughout the matrix, indicating the uniform formation of reaction products within the binder. The presence of Ca, Si and Al indicates a good confirmation of the formation of the C-(A)-S-H gel phase, which is known as the main binding phase for strength development in alkali-activated slag systems [75]. The microstructure of the M10 sample was slightly more heterogeneous than the control mixture (M0). This behavior may be attributed to the partial substitution of GBFS by $CaCO_3$-rich MS particles, which led to a decrease in the amount of reactive precursor for gel formation. However, the continuity of the C-(A)-S-H gel network was largely maintained, suggesting that the alkali-activation process remained effective at this replacement level. The homogeneous elemental distribution and the absence of pervasive microcracking indicate that the matrix retained good structural integrity with the addition of MS.

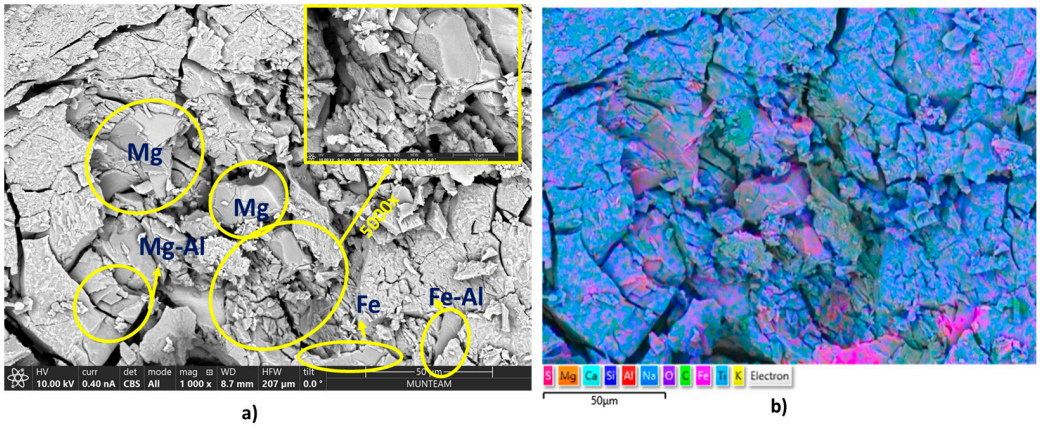


Figure 19. (**a**) SEM view and (**b**) EDS mapping results of M10 specimen (10% MS) cured for 28 days before F-T exposure.

The small reduction in compressive strength measured for the M10 mixture may be explained by the reduced GBFS content and the increased microstructural heterogeneity. Furthermore, localized pores and weak interfacial regions might have been formed due to the presence of partially unreacted MS particles in the matrix. These observations agree with the experimental higher values of porosity and water absorption. Therefore, the SEM/EDS results provide a microstructural explanation of the mechanical and durability performance of M10 mixture and support a moderate MS incorporation without a significant degradation of the binder matrix.

Figure 20 shows the elemental maps, where different colors were used to identify the distribution of each element: Al (red), C (light green), Ca (turquoise), Si (dark blue), O (purple), Na (light blue), Mg (orange), Fe (pink) and K (yellow). SEM-EDS mapping analysis showed that O, Ca, Si and Al are evenly distributed in the matrix. Such uniform distribution is indicative of the formation of a continuous and well-developed C-(A)-S-H gel network, which suggests that the alkali-activation reactions occurred throughout the binder matrix and not only in localized areas. In contrast, Na displayed a widely spread distribution

with some localized enrichment, which could be related to remaining alkali-rich phases or incomplete activator consumption. Mg was mainly found in clustered regions, which suggests it was part of the secondary reaction products rather than the primary binding gel. The inhomogeneous distribution of K, C and Fe suggests that they are found in isolated particles or in localized reaction zones in the matrix. Overall, the elemental mapping indicates a relatively homogenous binder composition, while the local presence of secondary elements accounts for the microstructural heterogeneity seen in the SEM images.

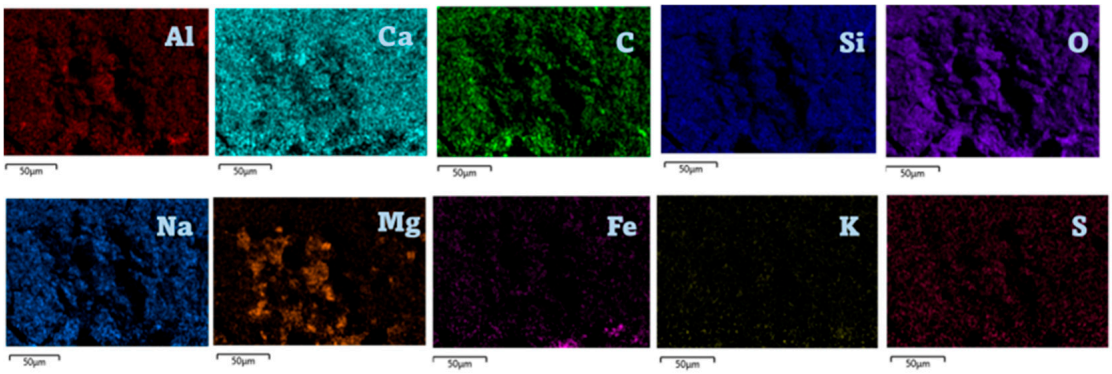


Figure 20. Elemental distribution of M10 (10% MS) cured for 28 days before F-T exposure.

EDS analysis of AAMS mixture with 10% MS (Figure 21) showed the major elements were O, Ca, Si and Al with weight percentages of 46.8%, 19.1%, 14.1% and 7.9%, respectively. The elemental composition shows that the main reaction product is C-(A)-S-H gel, which is in good agreement with the alkali activation mechanism of slag-based systems. The Ca/Si ratios of M0 and M10 were 1.08 and 1.35, respectively, which increased by about 26% after incorporation of MS. The increase is due to the rich $CaCO_3$ nature of mussel shell particles which indicate a calcium enriched gel structure. It has been shown earlier that the changes in pore structure and matrix porosity of C-(A)-S-H gels are strongly correlated with variations in the Ca/Si ratio [76]. Therefore, the higher Ca/Si ratio of M10 can explain its lower porosity and water absorption compared to mixtures with higher MS content. The Si/Al ratio also increased from 3.02 for M0 to 3.28 for M10, indicating a slightly higher degree of silicate polymerization and gel densification. The Si/Al ratio is a major parameter controlling the development of the gel network and the structural stability [77], so this increase is in accordance with the enhanced compressive strength of the M10 mixture, which reached approximately 52 MPa after 28 days.

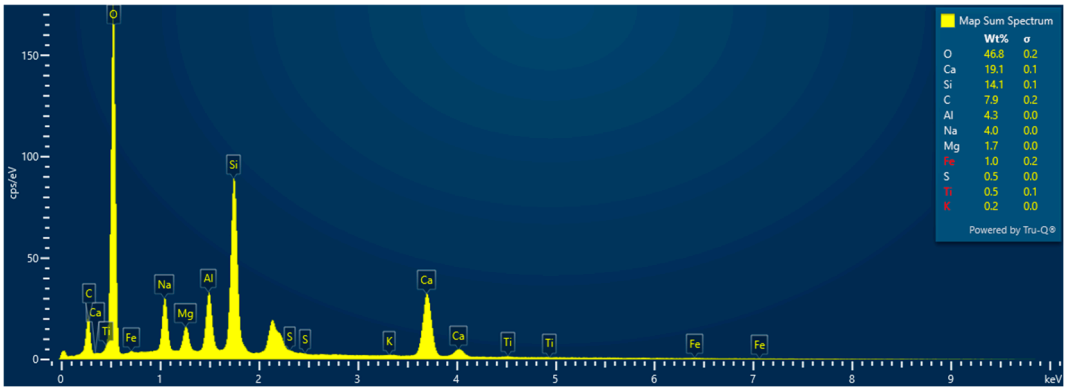


Figure 21. EDS picture of M10 mixing cured for 28 days before F-T exposure.

In general, the simultaneous increase in Ca/Si and Si/Al ratios indicates the formation of a denser and more stable C-(A)-S-H gel network. Such gel structures enriched with

calcium are known to refine the pore size distribution and to reduce the matrix porosity by forming a more compact hydration network [78]. These microstructural features are in good agreement with the macroscopic results, such as lower porosity and water absorption, higher compressive strength and better F-T resistance for the M10 mixture.

The results of the SEM/EDS mapping of the M0 specimen after 100 F-T cycles are shown in Figure 22a,b. SEM micrographs show the appearance of large micro-cracks and discontinuities in the matrix. In several areas the gel structures collapsed and broke up, suggesting that repeated freezing and thawing produced internal hydraulic and crystallization pressures caused by expansion of pore water. Similar degradation mechanisms have been observed for alkali-activated slag systems subjected to F-T cycles, where the volumetric expansion of frozen water leads to the initiation and propagation of cracks within the binder matrix [79]. The observed deterioration is closely related to the partial disintegration of the C-(A)-S-H gel phase, which is identified as the main load-bearing phase in alkali-activated slag binders. Previous studies have shown that the progressive degradation of the bonding capacity of C-(A)-S-H gels through increased pore connectivity and microstructural damage during F-T cycling leads to strength loss and durability reduction. In addition, the formation and propagation of microcracks allow water to enter the matrix, which promotes the subsequent F-T damage and creates a self-amplifying deterioration mechanism [80].

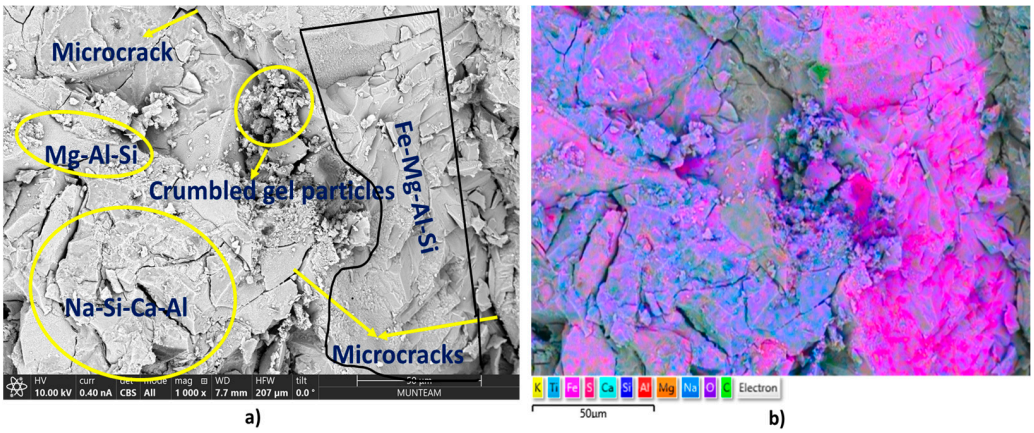


Figure 22. (**a**) SEM and (**b**) EDS mapping of M0 sample cured for 28 days after F-T cycles.

The microstructural observations are in good agreement with the mechanical test results obtained in the present study. The damage in the form of severe cracking and gel degradation suffered by the M0 specimen is directly responsible for the dramatic decrease in the compressive strength after exposure to F-T. On the other hand, mixtures with moderate contents of mussel shell showed a more stable microstructure and less strength loss, indicating that the modified pore structure and gel composition were involved in improving F-T resistance. Therefore, the SEM/EDS results confirm that the durability performance of the investigated mortars is strongly controlled by the preservation of the C-(A)-S-H gel network and the restriction of microcracking induced by F-T [81].

Figure 23 presents the detailed elemental mapping of sample M0 after 100 F-T cycles. Here, Al is colored red, Ca turquoise, O purple, Si dark blue, Mg orange, Na light blue, and Fe pink. In comparison to its condition prior to the F-T cycle, sample M0 demonstrates that the elements O, Si, and Al maintain their homogeneity; however, the Ca element displays heightened heterogeneity and is scattered in a fragmented fashion. Furthermore, it is observed that the Fe and Mg elements undergo local condensation in the matrix after F-T cycles, making the secondary phases even more visible. The element Na, however, exhibited a more irregular distribution within the matrix after F-T cycles.

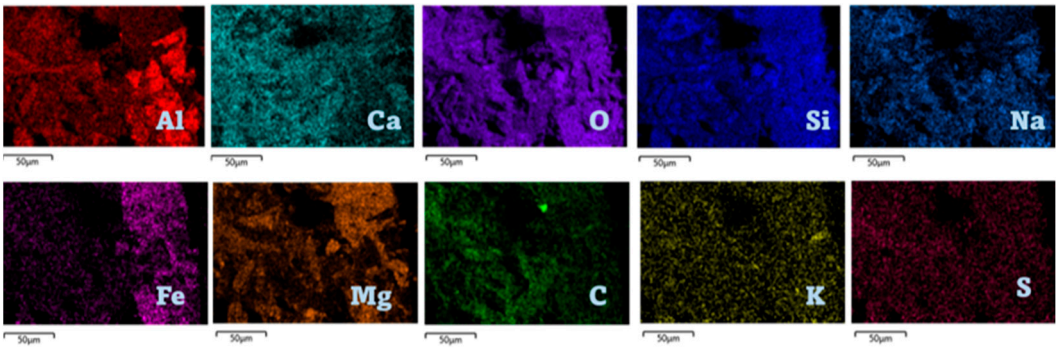


Figure 23. Elemental distribution of M0 mixing cured for 28 days after F-T cycles.

The EDS analysis of the M0 specimen after 100 F-T cycles is shown in Figure 24. The elemental composition was obtained: O (47.4%), Si (14.9%), Ca (13.6%), Al (5.4%), Mg (3.0%), Na (2.2%), Fe (2.7%) and K (0.2%). Consistent with the pre-freeze–thaw condition, Ca, O and Si remained the major elements, showing that the binder matrix was still primarily made up of C-(A)-S-H gel phases. The calculated Ca/Si and Si/Al ratios were 0.91 and 2.76, respectively. The reduction in the Ca/Si ratio compared with the corresponding values before F-T exposure indicates the partial depletion of calcium from the C-(A)-S-H gel structure. Previous studies have shown that a decrease in the Ca/Si ratio is related to gel decalcification, decreased structural stability, and degradation of the binding network [82]. This is consistent with the SEM images which showed extensive micro-cracking and discontinuities in the matrix after F-T cycling. Moreover, the relative increase in Mg and Fe contents suggests that the secondary phases were more prominent as the primary gel structure deteriorated. EDS mapping results support this interpretation and reveal a lesser homogeneity of elemental distribution than in the unexposed specimen. This expansion of pore water can produce hydraulic and crystallization pressure during repeated F-T cycles and thus cause formation and propagation of microcracks in the gel matrix. These cracks disrupt the continuity of the C-(A)-S-H network, increase the pore connectivity and allow further water ingress.

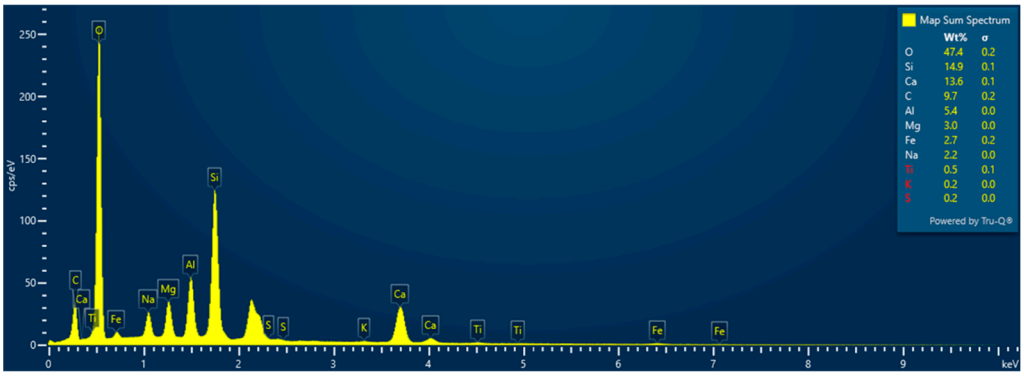


Figure 24. EDS spectrum of M0 cured for 28 days after F-T exposure.

The SEM/EDS-observed microstructural degradation gives a direct answer for the large decrease in compressive strength shown in Figure 15. Therefore, the decrease in Ca/Si ratio, the increased presence of secondary phases, and the severe microcracking altogether indicate that the freeze–thaw exposure gradually deteriorates the binding gel network and negatively affects the mechanical performance of the M0 mixture.

SEM morphology of the AAMS sample containing 10% MS after 100 F-T cycles is shown in Figure 25a,b. The SEM images show the presence of densely packed needle and rod-like crystalline formations distributed in the binder matrix. These calcium-rich

crystalline structures are associated with phases containing $CaCO_3$ from mussel shell particles and appear to be well incorporated in the surrounding C-(A)-S-H gel network. On the other hand, in the case of the M10 matrix, no significant microcracking was detected in the matrix after F-T exposure, unlike the case of the M0 specimen. The presence of interlocking needle-like crystals and the maintenance of gel continuity indicate that these phases were involved in the structural integrity of the matrix. Moreover, secondary Mg-Al-rich phases were observed inside the gel structure suggesting the formation of secondary reaction products which could contribute to the enhancement of the matrix stability. The microstructure observed corresponds to the improved F-T performance of the M10 mixture. The combination of the compact gel network and the reinforcing effect of the crystalline phases reduced the propagation of cracks and limited the damage induced by F-T. The lower strength loss and better durability performance of M10 than the reference mixture supports this interpretation. Thus, the SEM observations provide a microstructural explanation of the enhanced resistance of the 10% MS mixture to cyclic freezing and thawing.

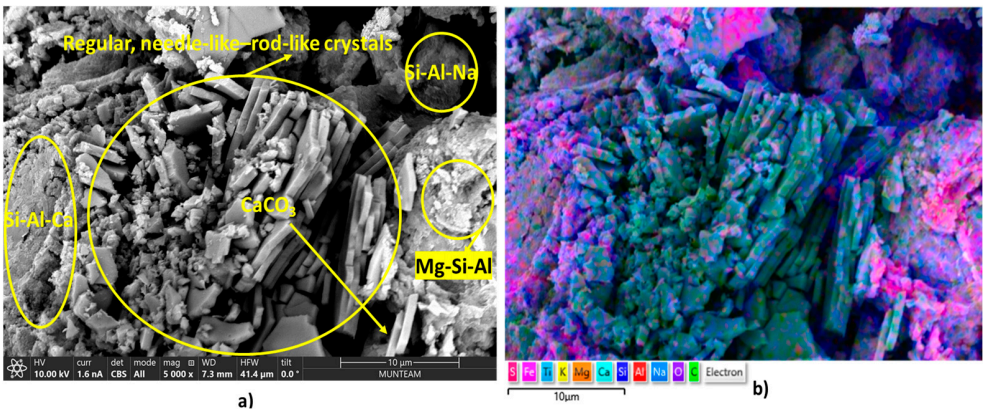


Figure 25. (**a**) SEM (**b**) EDS mapping image of M10 mixture (for cured 28 days) after F-T cycles.

Figure 26 shows that the elements are concentrated in needle-shaped crystals of Ca, shown in turquoise, but the Si and Al elements exhibit a similarly homogeneous distribution around the matrix. This verifies that the needle-like formations are calcium-rich phases and that the microstructure exhibits characteristics of C-(A)-S-H gel [83]. Mg was concentrated in distinct areas; whereas Fe had a confined, low-density distribution. The extensive presence of Na in the matrix signifies that activation has predominantly transpired. The findings indicate that 10% MS preserves gel continuity following F-T cycles, has a reduced number of microcracks, and exhibits a more resilient microstructure against F-T cycles in comparison to 0% MS.

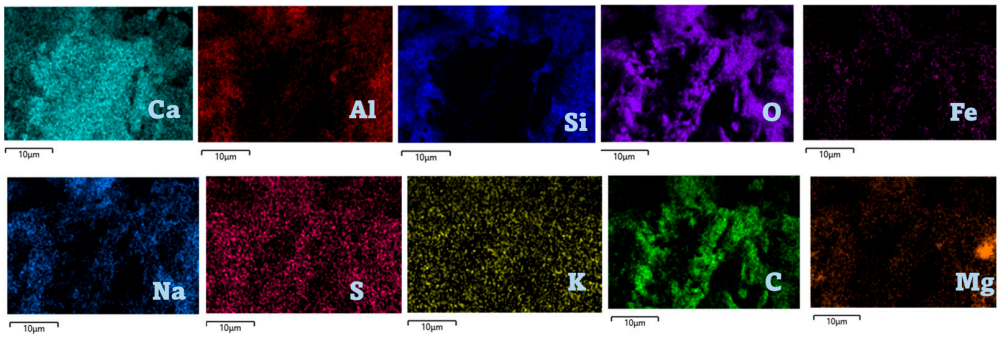


Figure 26. Elemental distribution of specimen M10 (for cured 28 days) after F-T exposure.

MS, a biogenic material with a high content of calcium carbonate, positively influences the microstructure, porosity, phase formation and, therefore, the mechanical and physical

properties of the whole system. The possible filling and nucleation role of the MS particles have also been discussed with the help of SEM and XRD results.

Figure 27 shows the EDS spectrum of the AAMS mixture with 10% MS and 90% GBFS after 100 freeze–thaw cycles. The weight percentages of the elements O, Ca, C, Si, Al, Na, Mg, and Fe in the map sum spectra are 41.6%, 33.4%, 12.1%, 7.6%, 2.1%, 1.4%, 0.6%, and 0.7%, respectively. The dominance of Ca and C is consistent with the presence of $CaCO_3$-rich phases originating from mussel shell particles. This observation correlates well with the needle-like crystalline structures seen in the SEM images (Figure 25) and Ca-rich regions seen by EDS mapping. The analyzed area presented a lower content of Si and Al in comparison with M0 and pre-freeze–thaw M10 specimens. The reason for this reduction is the local enrichment of the selected region in Ca-rich crystalline phases that form a major part of the composition and somewhat obscure the contribution of the surrounding C-(A)-S-H gel. The resulting Ca/Si ratio was thus calculated to be 4.4, which is significantly higher than those obtained for normal C-(A)-S-H gels. Such a high ratio indicates the formation of calcium rich secondary phases besides the primary binding gel. Overall, SEM and EDS results indicated that the F-T exposure promoted precipitation and persistence of Ca-rich crystalline products in the matrix. The relatively intact microstructure observed in Figure 25 suggests that these phases contribute to the preservation of matrix continuity and restrict crack propagation. This interpretation is consistent with the improved F-T resistance and lower strength loss obtained for the M10 mixture in comparison with the reference specimen. Therefore, microstructural and compositional studies directly justify the superior durability performance of the mortar with 10% MS.

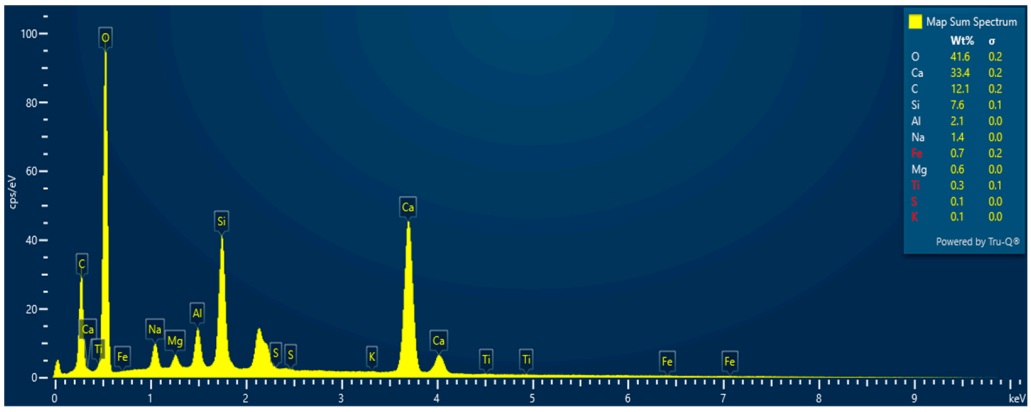


Figure 27. EDS spectrum values of sample M10 (for cured 28 days) after F-T cycles.

4. Conclusions

In this study, the potential use of mussel shell waste (MS) as a partial replacement of granulated blast furnace slag (GBFS) in alkali-activated mortars and its effect on fresh, mechanical, durability and microstructural properties were evaluated.

- The workability of the mixtures slightly decreased with the addition of MS. However, the flowability of all the mortars was acceptable, thus confirming that MS can be successfully included in alkali-activated systems without any significant effect on the fresh-state performance.
- The mechanical results showed that all the mixtures achieved compressive strengths higher than 45 MPa at 28 days, which confirmed the efficiency of the alkali-activated binder system. The increase in the MS content generally led to a decrease in strength, which was ascribed to the decrease in reactive GBFS and the increased microstructural heterogeneity. Despite this, the mixture containing 10% MS showed the most balanced performance in terms of strength and sustainability.

- Microstructural observations were in good agreement with the physical and durability properties. Increased MS replacement levels led to increased porosity, water absorption and capillary water uptake which were related to the presence of unreacted shell particles and a less homogeneous matrix structure. SEM/EDS analyses confirmed the formation of a continuous C-(A)-S-H gel network in all the mixes, and the mixes with higher MS contents showed increased heterogeneity and localized porous regions.
- The F-T tests showed that all mortars exhibited relatively low mass losses after 100 cycles, indicating good resistance to cyclic environmental exposure. Furthermore, the mixtures with MS showed better F-T behavior than the reference mixture, indicating the durability is improved by moderate incorporation of MS.

5. Limits of This Study and Recommendations

This investigation was constrained to mixture design parameters, a constant water/binder ratio, a constant activator ratio, and a maximum substitution of 20% MS. Future research may investigate varying alkali moduli (SiO_2/Na_2O), different NaOH molarities, and other activators (Na_2CO_3). Future research may examine sulfate attack, chloride penetration, carbonation depth, corrosion, and high-temperature tests. Furthermore, Life Cycle Assessment (LCA), CO_2 emission comparison, and energy consumption analysis will enhance the study's sustainability.

Funding: This research received no external funding.

Data Availability Statement: The data available in this study can be used upon request and citation.

Conflicts of Interest: The author declares no conflicts of interest.

Abbreviations

The following abbreviations are used in this manuscript:

AAMS	Alkali-Activated Mussel Shell/Slag Mortar
C-S-H	Calcium Silicate Hydrate
EDS	Energy-Dispersive X-ray spectroscopy analysis
EFNARC	European Federation for Specialist Construction Chemicals and Concrete Systems
F-T	Freeze–Thaw Testing
GBFS	Granulated Blast Furnace Slag
LCA	Life Cycle Assessment
MS	Mussel Shells
SEM	Scanning Electron Microscopy
UPV	Ultrasonic Pulse Velocity

References

1. Abiodun, Y.O.; Olanrewaju, O.A.; Gbenebor, O.P.; Ochulor, E.F.; Obasa, D.V.; Adeosun, S.O. Cutting Cement Industry CO_2 Emissions through Metakaolin Use in Construction. *Atmosphere* **2022**, *13*, 1494. [CrossRef]
2. Sultan, M.E.; Abo-El-Enein, S.A.; Sayed, A.Z.; EL-Sokkary, T.M.; Hammad, H.A. Incorporation of Cement Bypass Flue Dust in Fly Ash and Blast Furnace Slag-Based Geopolymer. *Case Stud. Constr. Mater.* **2018**, *8*, 315–322. [CrossRef]
3. Ramos, G.A.; de Matos, P.R.; Pelisser, F.; Gleize, P.J.P. Effect of Porcelain Tile Polishing Residue on Eco-Efficient Geopolymer: Rheological Performance of Pastes and Mortars. *J. Build. Eng.* **2020**, *32*, 101–699. [CrossRef]
4. Andrew, R.M. Global CO_2 Emissions from Cement Production, 1928-2018. *Earth Syst. Sci. Data* **2019**, *11*, 1675–1710. [CrossRef]
5. Deja, J.; Uliasz-Bochenczyk, A.; Mokrzycki, E. CO_2 Emissions from Polish Cement Industry. *Int. J. Greenh. Gas Control* **2010**, *4*, 583–588. [CrossRef]
6. de Oliveira, L.B.; de Azevedo, A.R.G.; Marvila, M.T.; Pereira, E.C.; Fediuk, R.; Vieira, C.M.F. Durability of Geopolymers with Industrial Waste. *Case Stud. Constr. Mater.* **2022**, *16*, e00839. [CrossRef]
7. Gao, T.; Shen, L.; Shen, M.; Chen, F.; Liu, L.; Gao, L. Analysis on Differences of Carbon Dioxide Emission from Cement Production and Their Major Determinants. *J. Clean. Prod.* **2015**, *103*, 160–170. [CrossRef]

8. Dinh, H.L.; Doh, J.H.; Liu, J.; Lu, L.; Song, H.; Park, D. Comprehensive Assessment of Geopolymer Concrete Mechanical and Environmental Performance with Glass Cullet Fine Aggregates. *J. Build. Eng.* **2023**, *76*, 107094. [CrossRef]
9. Çelikten, S.; Bayer Öztürk, Z.; Atabey, İ.İ. High-Temperature Resistance of Ceramic Sanitaryware Waste and Fly Ash-Based Geopolymer and Hybrid Geopolymer Mortars Produced at Ambient Curing Conditions. *Constr. Build. Mater.* **2024**, *446*, 137990.
10. Sharmin, S.; Sarker, P.K.; Biswas, W.K.; Abousnina, R.M.; Javed, U. Characterization of Waste Clay Brick Powder and Its Effect on the Mechanical Properties and Microstructure of Geopolymer Mortar. *Constr. Build. Mater.* **2024**, *412*, 134848. [CrossRef]
11. Pan, Z.; Tan, M.; Zheng, G.; Wei, L.; Tao, Z.; Hao, Y. Effect of Silica Fume Type on Rheology and Compressive Strength of Geopolymer Mortar. *Constr. Build. Mater.* **2024**, *430*, 136488. [CrossRef]
12. Beltrame, N.A.M.; Trisotto, A.V.; Souto, R.; da Silva, J.C.N.; Pereira, B.C.G.; Medeiros-Junior, R.A. Effect of Sulfate Attack on Geopolymer Mortars at Early Ages of Exposure. *Mater. Struct.* **2024**, *57*, 252. [CrossRef]
13. Cemalgil, S.; Gülmez, N.; Yön, M.Ş.; Karataş, M. Enhancing the Mechanical and Durability Properties of Fly Ash/GGBS-Based Geopolymer Mortars Using Dunite and Polypropylene Fibers. *Struct. Concr.* **2025**. [CrossRef]
14. Cemalgil, S.; Yön, M.Ş.; Dener, M.; Karataş, M. Mechanical and Durability Properties of Sustainable Alkali-Activated Mortars with Ceramic Insulator Waste and Andesite Powder as Partial Substitutes for GBFS. *Struct. Concr.* **2026**, *27*, 737–757. [CrossRef]
15. Chuewangkam, N.; Kidkhunthod, P.; Pinitsoontorn, S. Direct Evidence for the Mechanism of Early-Stage Geopolymerization Process. *Case Stud. Constr. Mater.* **2024**, *21*, e03539. [CrossRef]
16. Kolade, A.S.; Ikotun, B.D.; Oyejobi, D.O. A Review of the Chemistry, Waste Utilization, Mix Design and Performance Evaluation of Geopolymer Concrete. *Iran. J. Sci. Technol. Trans. Civ. Eng.* **2025**, *49*, 5421–5454. [CrossRef]
17. Mohan Kumar, S.G.K.; Kinuthia, J.M.; Oti, J.; Adeleke, B.O. Geopolymer Chemistry and Composition: A Comprehensive Review of Synthesis, Reaction Mechanisms, and Material Properties—Oriented with Sustainable Construction. *Materials* **2025**, *18*, 3823. [CrossRef] [PubMed]
18. Siyal, A.A.; Radin Mohamed, R.M.S.; Shamsuddin, R.; Ridzuan, M.B. A Comprehensive Review of Synthesis Kinetics and Formation Mechanism of Geopolymers. *RSC Adv.* **2024**, *14*, 446–462. [CrossRef] [PubMed]
19. El Alouani, M.; Saufi, H.; Aouan, B.; Bassam, R.; Alehyen, S.; Rachdi, Y.; El Hadki, H.; El Hadki, A.; Mabrouki, J.; Belaaouad, S.; et al. A Comprehensive Review of Synthesis, Characterization, and Applications of Aluminosilicate Materials-Based Geopolymers. *Environ. Adv.* **2024**, *16*, 100524. [CrossRef]
20. Frasson, B.J.; Rocha, J.C. Reaction Mechanism and Mechanical Properties of Geopolymer Based on Kaolinitic Coal Tailings. *Appl. Clay Sci.* **2023**, *233*, 106826. [CrossRef]
21. Jiang, T.; Liu, Z.; Tian, X.; Wu, J.; Wang, L. Review on the Impact of Metakaolin-Based Geopolymer's Reaction Chemistry, Nanostructure and Factors on Its Properties. *Constr. Build. Mater.* **2024**, *412*, 134760. [CrossRef]
22. Assaad, J.J.; Saba, M. Use of Seashell and Limestone Fillers in Metakaolin-Based Geopolymers for Masonry Mortars. *Minerals* **2023**, *13*, 186. [CrossRef]
23. Saba, M.; Fakhari Tehrani, F.; Hajikarimi, P.; Absi, J. Investigation on Partially Replacing Metakaolin with Marine Shell Waste to Produce Sustainable Eco-Friendly Geopolymer Mortars. *Clean Technol. Environ. Policy* **2023**, *25*, 2639–2653. [CrossRef]
24. Hasan, K.; Karim, A.; Islam, M.T.; Ali, M.B.; Rahman, M.T.; Rahman, M.M.; Yahaya, F.M. A Review of the Mechanical Properties and Durability of Concrete Containing Recycled Seashells as a Partial Cement Replacement. *J. Mater. Cycles Waste Manag.* **2023**, *25*, 3192–3216. [CrossRef]
25. Arslan, S.; Öz, A.; Benli, A.; Bayrak, B.; Kaplan, G.; Aydın, A.C. Sustainable Use of Silica Fume and Metakaolin in Slag/Fly Ash-Based Self-Compacting Geopolymer Composites: Fresh, Physico-Mechanical and Durability Properties. *Sustain. Chem. Pharm.* **2024**, *38*, 101512. [CrossRef]
26. Xing, Z.; Li, Z.; Wang, P.; Song, Z.; Wu, L. Research on the Mechanical Properties and Microstructure of Fly Ash, Slag, and Metakaolin Geopolymers. *Coatings* **2025**, *15*, 1258. [CrossRef]
27. Ergeshov, Z.; Örklemez, E.; Ketema, A.F.; Kwami, M.I.A.; Ilkentapar, S.; Durak, U.; Karahan, O.; Atis, C.D. Influence of Silica Fume on the Mechanical and Microstructural Properties and Life Cycle Assessment of Fly Ash-Based Geopolymer Mortar. *Arab. J. Sci. Eng.* **2026**, *51*, 4075–4092. [CrossRef]
28. Yön, M.Ş.; Arslan, F.; Karatas, M.; Benli, A. High-Temperature and Abrasion Resistance of Self-Compacting Mortars Incorporating Binary and Ternary Blends of Silica Fume and Slag. *Constr. Build. Mater.* **2022**, *355*, 129244. [CrossRef]
29. Stel'makh, S.A.; Shcherban', E.M.; Beskopylny, A.N.; Mailyan, L.R.; Meskhi, B.; Tashpulatov, S.S.; Chernil'nik, A.; Shcherban', N.; Tyutina, A. Composition, Technological, and Microstructural Aspects of Concrete Modified with Finely Ground Mussel Shell Powder. *Materials* **2023**, *16*, 82. [CrossRef] [PubMed]
30. Yanting, M.; Bo, D.; Xiaotong, Y.; Da, C.; Yingdi, L. Study on Mechanical Properties and Durability of Geopolymer Concrete with Oyster Shell Aggregate. *Constr. Build. Mater.* **2025**, *472*, 140926. [CrossRef]
31. Rihan, M.A.M.; Alahmari, T.S.; Onchiri, R.O.; Gathimba, N.; Sabuni, B. Impact of Alkaline Concentration on the Mechanical Properties of Geopolymer Concrete Made up of Fly Ash and Sugarcane Bagasse Ash. *Sustainability* **2024**, *16*, 2841. [CrossRef]

32. Picazo Camilo, E.; Carrillo Beltrán, R.; Valenzuela Expósito, J.J.; Perea Toledo, G.E.; Corpas Iglesias, F.A. Study of Olive Pomace Bottom Ashes as a Sustainable Alkaline Activator in the Syntesis of Geopolymers. *J. Build. Eng.* **2025**, *104*, 112383. [CrossRef]
33. Bellei, P.; Torres, I.; Solstad, R.; Flores-Colen, I. Potential Use of Oyster Shell Waste in the Composition of Construction Composites: A Review. *Buildings* **2023**, *13*, 1546. [CrossRef]
34. Bamigboye, G.; Enabulele, D.; Odetoyan, A.O.; Kareem, M.A.; Nworgu, A.; Bassey, D. Mechanical and Durability Assessment of Concrete Containing Seashells: A Review. *Cogent Eng.* **2021**, *8*. [CrossRef]
35. Leone, R.; Calà, A.; Capela, M.N.; Colajanni, S.; Campisi, T.; Saeli, M. Recycling Mussel Shells as Secondary Sources in Green Construction Materials: A Preliminary Assessment. *Sustainability* **2023**, *15*, 3547. [CrossRef]
36. Singh, V.K.; Srivastava, G. Development of a Sustainable Geopolymer Using Blast Furnace Slag and Lithium Hydroxide. *Sustain. Mater. Technol.* **2024**, *40*, e00934. [CrossRef]
37. Işıkdağ, B.; Mutlu, H.A. Durability of Non-Heat-Cured Geopolymer Mortars Containing Metakaolin and Ground Granulated Blast Furnace Slag. *Minerals* **2024**, *14*, 776. [CrossRef]
38. Alonso, A.A.; Álvarez-Salgado, X.A.; Antelo, L.T. Assessing the Impact of Bivalve Aquaculture on the Carbon Circular Economy. *J. Clean. Prod.* **2021**, *279*, 123873. [CrossRef]
39. Monneron-Gyurits, M.; Joussein, E.; Soubrand, M.; Fondanèche, P.; Rossignol, S. Valorization of Mussel and Oyster Shells toward Metakaolin-Based Alkaline Activated Material. *Appl. Clay Sci.* **2018**, *162*, 15–26. [CrossRef]
40. Hay, R.; Peng, B.; Celik, K. Filler Effects of CaCO3 Polymorphs Derived from Limestone and Seashell on Hydration and Carbonation of Reactive Magnesium Oxide (MgO) Cement (RMC). *Cem. Concr. Res.* **2023**, *164*, 107040. [CrossRef]
41. Fante, M.; Ribeiro, F.R.C.; Nunes, D.B.; Modolo, R.C.E.; Kazmierczak, C.d.S.; Mancio, M.; Tognoli, F.M.W.; de Azevedo, A.R.G.; Kulakowski, M.P. Behavior of Cementitious Mixtures with Filler Carbonate Subjected to Accelerated Carbonation. *Case Stud. Constr. Mater.* **2022**, *17*, e01300. [CrossRef]
42. Rux, K.; Tuen, M.; Suraneni, P. Utilization of Common Shell Wastes as a Limestone Alternative in Cementitious Materials. *Mater. Struct.* **2025**, *58*, 305. [CrossRef]
43. Hadjadj, M.; Guendouz, M.; Boukhelkhal, D. The Effect of Using Seashells as Cementitious Bio-Material and Granite Industrial Waste as Fine Aggregate on Mechanical and Durability Properties of Green Flowable Sand Concrete. *J. Build. Eng.* **2024**, *87*, 108968. [CrossRef]
44. Zhou, M.; Chen, J.; Huang, W.; Chao, H.; Yu, L.; Ma, X.; Ouyang, X. Multiscale Study on the Effect of Seashell Powder on Rheology, Hydration and Strength Development of Cement Paste. *Constr. Build. Mater.* **2024**, *456*, 139257. [CrossRef]
45. Liu, R.; Fan, J.; Yu, X.; Zhu, Y.; Chen, D. Properties of Mortar Containing Polyvinyl Alcohol Pretreated Waste Oyster Shells with Various Concentrations. *Constr. Build. Mater.* **2023**, *363*, 129879. [CrossRef]
46. Chen, B.; Peng, L.; Zhong, H.; Zhao, Y.; Meng, T.; Zhang, B. Synergetic Recycling of Recycled Concrete Aggregate and Waste Mussel Shell in Concrete: Mechanical Properties, Durability and Microstructure. *Constr. Build. Mater.* **2023**, *371*, 130825. [CrossRef]
47. Wang, K.; Fu, J.X.; Wang, J.; Li, Y. Assessing the Hydration Behavior of Rice Husk and Shell Ashes as Supplementary Cementitious Materials during Initial Curing Stages. *Constr. Build. Mater.* **2025**, *491*, 142773. [CrossRef]
48. *TS-EN-934-2*; Admixtures for Concrete, Mortar and Grout—Part 2: Concrete Admixtures—Definitions, Requirements, Conformity, Marking and Labelling. Turkish Standards Institution (TSE): Ankara, Türkiye, 2011.
49. Vitale, E.; Pesce, P.G.; Petti, R.; Russo, G.; Plötze, M.; Puzrin, A.; Vitone, C. Towards Bio-Sourced Solutions for Soil Treatment: Experimental Study on Seashell Powder as Precursor for Alkali-Activated Binders. *Biogeotechnics* **2025**, 100198. [CrossRef]
50. Şahin Yön, M.; Cemalgil, S. Impact of Basalt Powder on the Physical, Fresh, Hardened and Microstructural Characteristics of Granulated Blast Furnace Slag-Based Alkali-Activated Mortars. *Sak. Univ. J. Sci.* **2026**, *30*, 47–61. [CrossRef]
51. EFNARC (European Federation of Specialist Construction Chemicals and Concrete Systems). The European Guidelines for Selfcompacting Concrete: Specification, Production and Use, U.K, 2002. *Mag. Concr. Res.* **2002**, *64*, 401–409.
52. Suwan, T.; Fan, M. Influence of OPC Replacement and Manufacturing Procedures on the Properties of Self-Cured Geopolymer. *Constr. Build. Mater.* **2014**, *73*, 551–561. [CrossRef]
53. *ASTM C349*; Standard Test Method for Compressive Strength of Hydraulic-Cement Mortars (Using Portions of Prisms Broken in Flexure). ASTM International: West Conshohocken, PA, USA, 2002; pp. 1–6.
54. ASTM International. ASTM C 1585 04: Standard Test Method for Measurement of Rate of Absorption of Water by Hydraulic-Cement Concretes. In *American Society for Testing and Materials*; ASTM: West Conshohocken, PA, USA, 2007; pp. 1–6.
55. ASTM. ASTM C348 Flexural Strength of Hydraulic-Cement Mortars. In *American Society for Testing and Material*; ASTM: West Conshohocken, PA, USA, 2002; Volume 04, pp. 1–6.
56. *ASTM C 666/C 666M*; Standard Test Method for Resistance of Concrete to Rapid Freezing and Thawing 1. ASTM: West Conshohocken, PA, USA, 2003.
57. ASTM. ASTM C597-02 standard test method for pulse velocity through concrete. In *Annual Book of American Society of Testing and Materials*; ASTM: West Conshohocken, PA, USA, 2002; Volume 4.
58. Hasnaoui, A.; Bourguiba, A.; El Mendili, Y.; Sebaibi, N.; Boutouil, M. A Preliminary Investigation of a Novel Mortar Based on Alkali-Activated Seashell Waste Powder. *Powder Technol.* **2021**, *389*, 471–481. [CrossRef]

59. Wu, Y.; Lu, J.; Nie, Y.; He, W. Effect of Seashell Powder as Binder Material on the Performance and Microstructure of Low-Carbon Sustainable Alkali-Activated Concrete. *J. Build. Eng.* **2024**, *90*, 109442. [CrossRef]
60. Okoro, W.; Oyebisi, S. Mechanical and Durability Assessments of Steel Slag-Seashell Powder-Based Geopolymer Concrete. *Heliyon* **2023**, *9*, e13188. [CrossRef] [PubMed]
61. Maglad, A.M.; Othuman Mydin, M.A.; Dip Datta, S.; Tayeh, B.A. Assessing the Mechanical, Durability, Thermal and Microstructural Properties of Sea Shell Ash Based Lightweight Foamed Concrete. *Constr. Build. Mater.* **2023**, *402*, 133018. [CrossRef]
62. Artismo, T.V.; Braga, F.d.O.; Rocha, C.A.A. Physical-Mechanical Behavior of Workable Mortars with Perna Perna Mussel Shell as Fine Aggregate. *Constr. Build. Mater.* **2024**, *418*, 135411. [CrossRef]
63. Khatib, J.M.; Herki, B.A.; Kenai, S. Capillarity of Concrete Incorporating Waste Foundry Sand. *Constr. Build. Mater.* **2013**, *47*, 867–871. [CrossRef]
64. Sheshadri, A.; Marathe, S.; Sadowski, Ł. Development of Sustainable, High Strength Slag Based Alkali Activated Pavement Quality Concrete Using Agro-Industrial Wastes: Properties and Life Cycle Analysis. *Int. J. Pavement Eng.* **2024**, *25*, 2410953. [CrossRef]
65. Rashad, A.M.; Morsi, W.M.; Khafaga, S.A. Effect of Limestone Powder on Mechanical Strength, Durability and Drying Shrinkage of Alkali-Activated Slag Pastes. *Innov. Infrastruct. Solut.* **2021**, *6*, 127. [CrossRef]
66. Hailemariam, B.Z.; Yehualaw, M.D.; Taffese, W.Z.; Vo, D.H. Optimizing Alkali-Activated Mortars with Steel Slag and Eggshell Powder. *Buildings* **2024**, *14*, 2336. [CrossRef]
67. Keskinkılınç, M.K.; Yıldız, S.; Eronat, Ş.S.; Emiroğlu, M. Investigation of Alkali Activated Ferrochromium Slag Composites Including Waste Marble Powder. *Sak. Univ. J. Sci.* **2024**, *28*, 654–667. [CrossRef]
68. Huang, M.; Bao, S.; Zhang, Y.; Li, M.; Ping, Y.; Lin, C. Durability of Alkali-Activated Cementitious Materials at Freeze-Thaw Environment: Damage and Protection Mechanism. *Constr. Build. Mater.* **2025**, *488*, 142102. [CrossRef]
69. Hamzah, H.K.; Huseien, G.F.; Asaad, M.A.; Georgescu, D.P.; Ghoshal, S.K.; Alrshoudi, F. Effect of Waste Glass Bottles-Derived Nanopowder as Slag Replacement on Mortars with Alkali Activation: Durability Characteristics. *Case Stud. Constr. Mater.* **2021**, *15*, e00775. [CrossRef]
70. Cui, Y.; Ye, D.; Bai, W.; Guan, J.; Yuan, C.; Xie, C.; Li, L. Multi-Scale Damage Degradation Mechanism and Constitutive Behavior of Alkali-Activated Slag-Based Concrete under Freeze-Thaw Environments. *Constr. Build. Mater.* **2025**, *493*, 143305. [CrossRef]
71. Zhang, Y.; He, Y.; Cui, X.; Liu, L. Enhancing Freeze-Thaw Resistance of Alkali-Activated Slag by Metakaolin. *ACS Omega* **2023**, *8*, 20869–20880. [PubMed]
72. Chen, B.; Wang, J. Experimental Study on the Durability of Alkali-Activated Slag Concrete after Freeze-Thaw Cycle. *Adv. Mater. Sci. Eng.* **2021**, *2021*, 9915639. [CrossRef]
73. Yön, M.Ş.; Karataş, M. Evaluation of the Mechanical Properties and Durability of Self-Compacting Alkali-Activated Mortar Made from Boron Waste and Granulated Blast Furnace Slag. *J. Build. Eng.* **2022**, *61*, 105263.
74. Kamath, M.; Prashant, S.; Ralegaonkar, R. Microstructure Properties of Popular Alkali-Activated Pastes Cured in Ambient Temperature. *Buildings* **2023**, *13*, 858. [CrossRef]
75. He, J.; Yu, S.; Sang, G.; He, J.; Wang, J.; Chen, Z. Properties of Alkali-Activated Slag Cement Activated by Weakly Alkaline Activator. *Materials* **2023**, *16*, 3871. [CrossRef] [PubMed]
76. Han, F.; Zhu, Z.; Zhang, H.; Li, Y.; Fu, T. Effect of Steel Slag on the Properties of Alkali-Activated Slag Material: A Comparative Study with Fly Ash. *Materials* **2024**, *17*, 2495. [CrossRef] [PubMed]
77. Hu, M.; Chen, J.; Xia, B.; Chen, J. The Governing Role of Si/Al Ratio in the Structural Evolution and Mechanical Properties of N-A-S-H Gel. *Materials* **2026**, *19*, 246. [PubMed]
78. Lv, Y.; Wang, C.; Han, W.; Li, X.; Peng, H. Study of the Mechanical Properties and Microstructure of Alkali-Activated Fly Ash–Slag Composite Cementitious Materials. *Polymers* **2023**, *15*, 1903. [PubMed]
79. Fu, Y.; Cai, L.; Yonggen, W. Freeze-Thaw Cycle Test and Damage Mechanics Models of Alkali-Activated Slag Concrete. *Constr. Build. Mater.* **2011**, *25*, 3144–3148.
80. Zhu, J.; Li, Z.; Huang, Y.; Li, Y.; Huang, Y.; Min, H. Experimental Study on the Coupling of Freeze-Thaw Cycle and Chloride Corrosion of Alkali Slag Cementitious Materials. *Polymers* **2025**, *17*, 1474. [CrossRef] [PubMed]
81. Provis, J.L.; Palomo, A.; Shi, C. Advances in Understanding Alkali-Activated Materials. *Cem. Concr. Res.* **2015**, *78*, 110–125. [CrossRef]
82. Provis, J.L.; Bernal, S.A. Geopolymers and Related Alkali-Activated Materials. *Annu. Rev. Mater. Res.* **2014**, *44*, 299–327. [CrossRef]
83. Vázquez-Rodríguez, F.; Elizondo, N.; Montes-González, M.; Gómez-Rodríguez, C.; González-Carranza, Y.; Guzmán, A.M.; Rodríguez, E.A. Microstructural and Mechanical Characteristics of Alkali-Activated Binders Composed of Milled Fly Ash and Granulated Blast Furnace Slag with μ-Limestone Addition. *Materials* **2023**, *16*, 3818. [PubMed]

Disclaimer/Publisher's Note: The statements, opinions and data contained in all publications are solely those of the individual author(s) and contributor(s) and not of MDPI and/or the editor(s). MDPI and/or the editor(s) disclaim responsibility for any injury to people or property resulting from any ideas, methods, instructions or products referred to in the content.